NUREG/CR-1347
ORNL/NUREG-62

ornl

OAK RIDGE NATIONAL LABORATORY

UNION CARBIDE

Thermocouple Signal Sensitivity to the Sheath Thickness of Thermal-Hydraulic Test Facility Indirectly Heated Electric Fuel Pin Simulators

R. D. Dabbs L. J. Ott

Prepared for the U.S. Nuclear Regulatory Commission
Office of Nuclear Regulatory Research
Under Interagency Agreements DOE 40-551-75 and 40-552-75

OPERATED BY
UNION CARBIDE CORPORATION
FOR THE UNITED STATES
DEPARTMENT OF ENERGY

Printed in the United States of America. Available from
National Technical Information Service
U.S. Department of Commerce
5285 Port Royal Road, Springfield, Virginia 22161

Available from

GPO Sales Program
Division of Technical Information and Document Control
U.S. Nuclear Regulatory Commission
Washington, D.C. 20555

NUREG/CR-1347
ORNL/NUREG-62
Dist. Category R2

Contract No. W-7405-eng-26

Engineering Technology Division

THERMOCOUPLE SIGNAL SENSITIVITY TO THE SHEATH THICKNESS OF THERMAL-HYDRAULIC TEST FACILITY INDIRECTLY HEATED ELECTRIC FUEL PIN SIMULATORS

R. D. Dabbs L. J. Ott

Manuscript Completed—July 16, 1980
Date Published—August 1980

Prepared for the U.S. Nuclear Regulatory Commission
Office of Nuclear Regulatory Research
Under Interagency Agreements DOE 40-551-75 and 40-552-75

NRC FIN No. B0125

Prepared by the
OAK RIDGE NATIONAL LABORATORY
Oak Ridge, Tennessee 37830
operated by
UNION CARBIDE CORPORATION
for the
DEPARTMENT OF ENERGY

CONTENTS

Page

LIST OF FIGURES v

LIST OF TABLES vii

LIST OF CONVERSIONS ix

SUMMARY xi

ABSTRACT 1

1. INTRODUCTION 1

2. REPORT OBJECTIVES 6

3. THERMOCOUPLE FREQUENCY STUDY (TFS) 7

3.1 Forward-Implicit Version of ORINC 7

3.2 Test Matrix Formulation 9

3.3 Period-Depth Correlation: Power Zone I 14

3.4 Period-Depth Correlation: Power Zone V 18

3.5 Period-Depth Composite Relationship 19

4. THERMOCOUPLE RESPONSE STUDY (TRS) 21

4.1 Test Matrix Formulation 21

4.2 Radial Time Constant Determination 23

4.3 Time Response–Depth Composite Relationship 27

5. CONCLUSIONS AND RECOMMENDATIONS 35

REFERENCES 39

APPENDIX A. A STEP-RESPONSE SOLUTION TO THE GOVERNING DIFFERENTIAL EQUATION OF A FIRST-ORDER DYNAMIC SYSTEM 43

APPENDIX B. THE DETERMINATION OF AN EFPS HIGHER-ORDER RESPONSE FUNCTION STRUCTURE 47

List of Figures

Number		Page
1.1	Indirectly heated EFPS assembly.	2
1.2	Indirectly heated bundle 1 or bundle 2 fuel pin simulator cross section.	3
1.3	Location of axial power zones and their local-to-average heat generation rates for bundle 1 or bundle 2 EFPS.	4
1.4	Idealized EFPS segment construction details showing regional compositions and locations of the dimensions listed in Table 1.1.	5
3.1	ORINC model (one-dimensional along chain-dashed line) for bundle 2 EFPS. Axial power zone V is represented by the 16-node model, and axial power zone 1 is represented by the 14-node model.	8
3.2	Heat transfer coefficient square-wave boundary condition as constructed using 20 data points per cycle.	10
3.3	Heat transfer coefficient boundary condition for case TFS1 involving axial power zone V.	11
3.4	Heat transfer coefficient boundary condition for case TFS4 involving axial power zone V.	12
3.5	Heat transfer coefficient boundary condition for case TFS7 involving axial power zone V.	12
3.6	Representation of thermocouple frequency resolution analysis incorporating the nodal COM trend temperature (- - -), the mean oscillation amplitude α (——), and the trend standard deviation σ (- - -) bands.	13
3.7	NOD10 COM temperature and its associated mean oscillation amplitude and trend standard deviation bands. Calculations correspond to case TFS1 and axial power zone I.	15
3.8	NOD11 COM temperature and its associated mean oscillation amplitude and trend standard deviation bands. Calculations correspond to case TFS1 and axial power zone I.	15
3.9	NOD12 COM temperature and its associated mean oscillation amplitude and trend standard deviation bands. Calculations correspond to case TFS1 and axial power zone I.	16
3.10	NOD13 COM temperature and its associated mean oscillation amplitude and trend standard deviation bands. Calculations correspond to case TFS1 and axial power zone I.	16
3.11	EFPS centerline temperature and its associated mean oscillation amplitude and trend standard deviation bands. Calculations correspond to case TFS1 and axial power zone I.	17
3.12	EFPS surface temperature and its associated mean oscillation amplitude and trend standard deviation bands. Calculations correspond to case TFS1 and axial power zone I.	17

3.13	Calculated EFPS surface heat flux corresponding to case TFS1 and axial power zone I.	18
3.14	Desirable combinations (represented by crosshatched area) of thermocouple bead depth and surface phenomenon period as determined by cases TFS1 through TFS7 involving axial power zone I.	19
3.15	Desirable combinations (represented by crosshatched area) of thermocouple bead depth and surface phenomenon period as determined by cases TFS1 through TFS7 involving axial power zone V.	20
4.1	First-order time-response relationship between τ and $(T_\infty - T_i)$ for $T_\infty < T_i$ at a given radial position.	25
4.2	First-order time-response relationship between τ and $(T_\infty - T_i)$ for $T_\infty > T_i$ at a given radial position.	25
4.3	Relationship between surface or centerline first-order time constants and transient heat transfer coefficients for cases TRS01 through TRS22.	29
4.4	Relationship between surface or centerline first-order time constants and transient heat transfer coefficients with prediction from Eq. (4.10).	31
4.5	A representation of radially dependent first-order time constants for a cooling EFPS experiencing dominating surface-heat flux driving potential.	33
5.1	Desirable combinations (represented by crosshatched area) of thermocouple bead depth and surface phenomenon period as determined by cases TFS1 through TFS7 involving axial power zone I.	36
5.2	Desirable combinations (represented by crosshatched area) of thermocouple bead depth and surface phenomenon period as determined by cases TFS1 through TFS7 involving axial power zone V.	37
B.1	Simplified EFPS model used in determining higher-order response function structure.	48

List of Tables

Number		Page
1.1	Radial dimensions of bundle 2 EFPS at axial power zones I and V.	4
3.1	Radial dimension information for ORINC model of bundle 2 EFPS at axial level corresponding to power zone I.	8
3.2	Radial dimension information for ORINC model of bundle 2 EFPS at axial level corresponding to power zone V.	9
3.3	Steady-state boundary conditions for all TFS cases.	10
3.4	TFS cases and their corresponding heat transfer coefficient square-wave periods.	10
3.5	Calculational timestep and transient duration information for all TFS cases.	11
3.6	Thermocouple frequency resolution analysis results for axial power zone I.	14
3.7	Thermocouple frequency resolution analysis results for axial power zone V.	18
4.1	Steady-state ($t = 0$) boundary conditions and calculational timestep size for all TRS cases.	22
4.2	Transient ($0 < t \leq t_{end}$) boundary conditions and calculational timestep size for all TRS cases.	23
4.3	EFPS centerline and EFPS surface first-order time constants with associated uncertainties for [illegible]RS cases.	26
4.4	Radially dependent first-order time constants (s) for selected TRS cases.	27
4.5	Critical information for determining radially dependent first-order time constants relative to case TRS03.	28

List of Conversions

Length	1 mil	$= 2.54 \times 10^{-2}$ mm
	1 mil	$= 2.54 \times 10^{-3}$ cm
	1 mil	$= 2.54 \times 10^{-5}$ m
	1 in.	= 25.4000 mm
	1 in.	= 2.5400 cm
	1 in.	$= 2.54 \times 10^{-2}$ m
	1 ft	= 304.8000 mm
	1 ft	= 30.4800 cm
	1 ft	= 0.3048 m
Temperature	°F	$= 1.8\ (K - 273.0) + 32.0$
	Δ°F	$= 0.5556\ \Delta K$
Heat transfer coefficient	1 Btu/(s·ft²·°F)	$= 20.4368$ kW/(m²·K)
	1 Btu/(h·ft²·°F)	$= 5.6768$ W/(m²·K)
Surface heat flux	1 Btu/(s·ft²)	$= 11.3538$ kW/m²
	1 Btu/(h·ft²)	$= 3.1538$ W/m²
Power generation density	1 Btu/(s·ft³)	$= 37.2499$ kW/m³
	1 Btu/(h·ft³)	$= 10.3472$ W/m³
Linear power generation	1 Btu/(s·ft)	$= 3.4607$ kW/m
	1 Btu/(h·ft)	$= 0.9613$ W/m
Power	1 Btu/s	= 1.0548 kW
	1 Btu/h	= 0.2929 W

SUMMARY

The distance that a thermocouple bead is located from the surface of an indirectly heated electric fuel pin simulator (EFPS) and the uncertainty of the thermocouple signal severely inhibit the ability of the thermocouple to accurately resolve high-frequency changes in the surface temperature. A thermocouple bead with a measurement standard deviation of 0.556 K and located 0.0508 mm below the surface [Thermal-Hydraulic Test Facility (THTF) bundle 1 EFPS design] was found capable of resolving surface phenomena occurring only at a period of >90 ms for a low-power axial zone and >40 ms for the highest-power axial zone. These are on the same order as the periods that the THTF data acquisition system can successfully resolve (~100 ms). Therefore, the loss of surface phenomena resolution (if any) is due to the limitations of the thermometry and not to the limitations of the data acquisition system.

The radially dependent thermocouple time response is dominated by the surface-heat-flux driving potential, which forces the mid- and outer-radius nodes to have first-order time constants almost identical to the first-order time constant of the surface. Because large surface heat fluxes frequently occur in the early part of a typical loss-of-coolant transient or during a rewet, the effect of radial position on the thermocouple time response is minimal for these time frames. Higher-order response theory for the thermal response of the EFPS was developed to establish that first-order response theory accurately predicts the radially dependent time constants for given ranges of heat transfer coefficients (h). Important results from the application of the higher-order response theory include the following:

1. Overall EFPS response (in all heat transfer regimes) cannot be predicted by first-order response theory.

2. For specific heat transfer coefficient ranges [$h < \sim 4\ kW/(m^2 \cdot K)$ and $h > \sim 11.4\ kW/(m^2 \cdot K)$], the EFPS surface behaves in a first-order fashion.

3. In cases dominated by surface heat transfer resistance [$h < \sim 4\ kW/(m^2 \cdot K)$], the total EFPS time constant can be approximated by

$$\tau = [(\rho C_p V)_{EFPS}]/(h 2\pi \ell r_{surface}) ,$$

where

$(\rho C_p V)_{EFPS}$ = capacitance of EFPS for thermal energy,

ℓ = axial length of EFPS,

$r_{surface}$ = outer radius of EFPS.

Even for these cases, the differences between the centerline and surface response times are 1.3 to 2.0 s.

4. When an internal thermal resistance dominates [$h > \sim 11.4\ kW/(m^2 \cdot K)$], the EFPS surface responds much faster than predicted by the above equation, and the centerline response appears to be totally independent of the heat transfer coefficient.

5. The centerline response is multiorder, but for high surface heat transfer coefficients the centerline response time asymptotically approaches

$$\tau_{\ell} = \rho_{MGO}\, C_{p_{MGO}} r_{MGO}^2/(4K_{MGO}) ,$$

where

ρ_{MGO} = density of magnesium oxide core,

$C_{P_{MGO}}$ = specific heat of magnesium oxide core,

r_{MGO} = outer radius of magnesium oxide core,

K_{MGO} = thermal conductivity of magnesium oxide core.

6. In certain situations—defined by high surface heat fluxes—the first-order response times of radial positions inside the EFPS are shorter than the EFPS surface response time.

7. The EFPS response is highly dependent on initial conditions and on the combination of forcing functions at the surface (i.e., the heat transfer coefficient and sink temperature).

8. The EFPS response is not strongly dependent on the change in EFPS geometries from one axial power zone to another axial power zone.

Future EFPSs should have a sheath (assuming the thermocouple resides within the inner surface of this sheath) as thin as mechanically possible and preferably not in excess of 0.254 mm. An extensive effort should also be made to reduce as well as to determine more accurately the thermocouple signal uncertainty (i.e., measurement standard deviation). These factors would greatly reduce the uncertainties found in the numerical EFPS analysis which uses the thermocouple signal as a foundation.

THERMOCOUPLE SIGNAL SENSITIVITY TO THE SHEATH THICKNESS OF THERMAL-HYDRAULIC TEST FACILITY INDIRECTLY HEATED ELECTRIC FUEL PIN SIMULATORS

R. D. Dabbs L. J. Ott

ABSTRACT

Analysis of data in large loss-of-coolant accident experimental facilities often requires extensive use of signals recorded from thermocouples embedded in indirectly heated electric fuel pin simulators (EFPS). These signals, converted to temperature, are used in the numerical determination of EFPS experimental conditions, including transient surface temperature, transient surface heat flux, and transient internal radial temperature distribution.

Important points that arise in using the recorded thermocouple signals as a basis for subsequent analysis include (1) the effect of the distance that the thermocouple bead is located from the EFPS surface on the ability of the thermocouple to resolve rapidly changing boundary phenomena and (2) the extent that this depth influences the time response associated with the thermocouple. Several numerically solved EFPS transients (where boundary conditions were specified, and surface temperature, surface heat flux, and internal radial temperature histories were subsequently calculated) are presented in an effort to establish these two relationships and to form a foundation for recommending designs which will minimize the adverse effects of these relationships by specifying optimal thermocouple radial positions in future EFPSs.

1. INTRODUCTION

The Oak Ridge National Laboratory (ORNL) Pressurized-Water Reactor Blowdown Heat Transfer Separate-Effects Program[1] comprises two major areas of investigation: (1) an experimental separate-effects study of the relations among the principal variables that can alter the rate of blowdown—the presence of flow reversal and rereversal, time delay to critical heat flux, the rate at which dryout progresses, and similar time- and space-related functions that are important to loss-of-coolant accident analysis—and (2) the development of a steady-state and transient heat transfer–local fluid condition data base applicable to bundle geometries. Data pertinent to these areas of investigation are obtained from the Thermal-Hydraulic Test Facility (THTF), a large nonnuclear experimental loop with a test section that employs a square array of indirectly heated electric fuel pin simulators (EFPSs) (Fig. 1.1).

The EFPSs in both bundle 1 and bundle 2* have a dual-sheath design, which is cross sectioned for two axial locations in Fig. 1.2. The outer and inner sheaths are stainless steel with the inner grooved to accept a 0.508-mm-OD Chromel-Alumel thermocouple. A boron nitride (BN) annulus inside the stainless steel sheaths electrically insulates the heating element from these sheaths. The heating element, an annulus located concentrically within the BN annulus, consists of an Inconel 600 base and a series of

*Bundle 1 and bundle 2 refer to the first and second EFPS bundles (7 × 7 arrays) designed for testing in the THTF. All THTF tests to date have been performed using bundle 1; though it has not been installed, bundle 2 will be used as a design basis for this study because of the increased total thickness of the stainless steel sheaths.

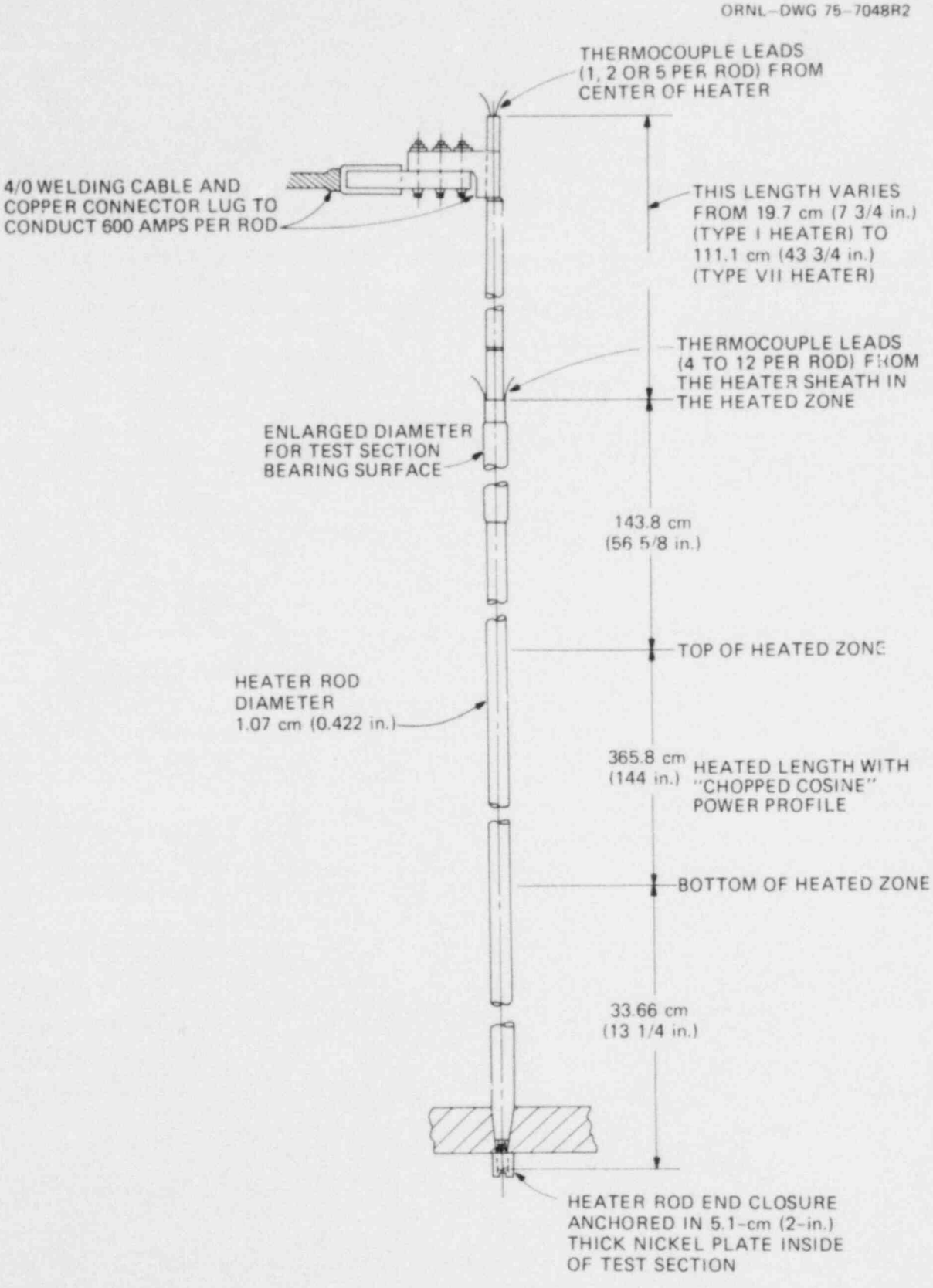

Fig. 1.1. Indirectly heated EFPS assembly.

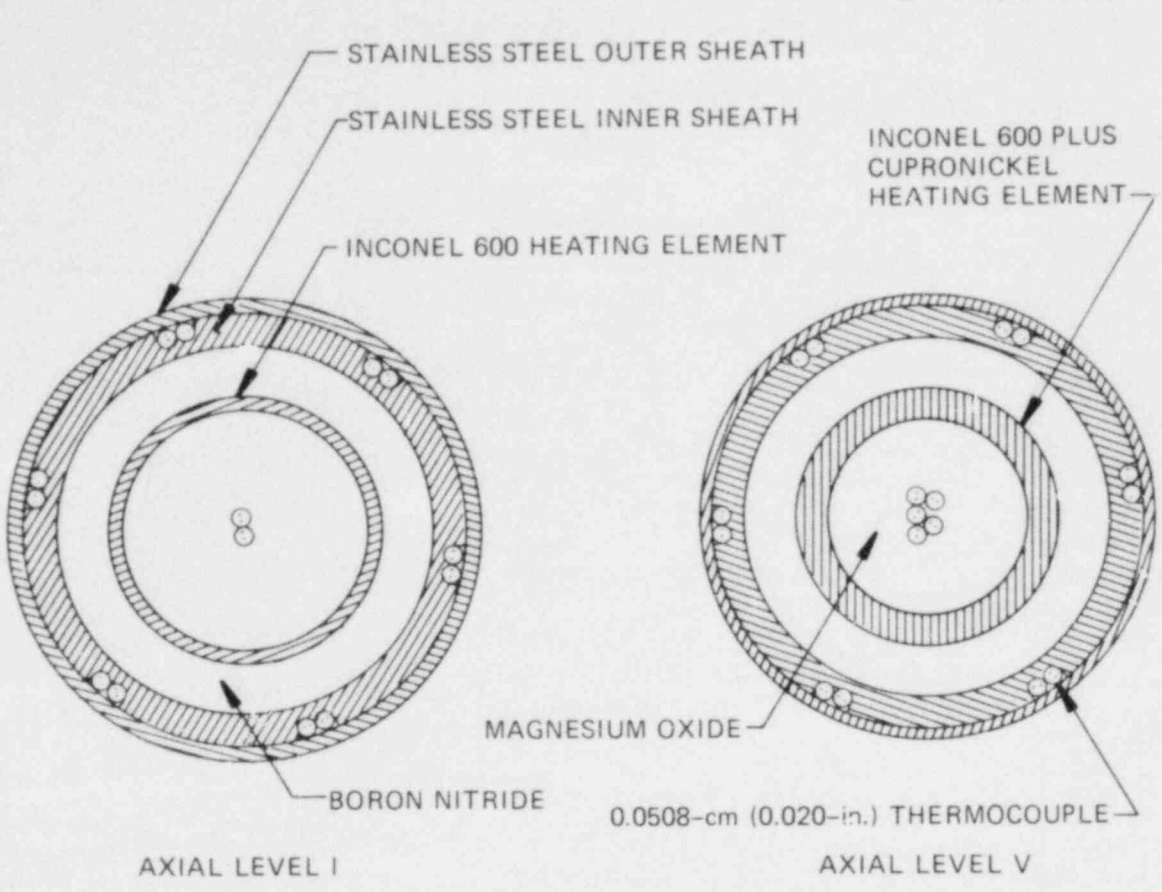

Fig. 1.2. Indirectly heated bundle 1 or bundle 2 fuel pin simulator cross section.

swaged cupronickel and/or Inconel 600 oversleeves which allow variable axial heat generation, thus creating the stepped-chopped-cosine axial power profile. The central axial region of the heating element, which has the highest electrical resistance and maximum heat generation rate, is composed of only the Inconel 600 base. Successive oversleeves of Inconel 600 or cupronickel are swaged over the base with each succeeding oversleeve extending to the end of the heating element. Oversleeves reduce the resistance of the heating element and therefore decrease the power generation rate of that axial region. The heated zone lengths and the representative axial power ratios for a prototypical THTF bundle 1 or bundle 2 fuel pin simulator are shown in Fig. 1.3. (The axial level I and axial level V cross sections in Fig. 1.2 correspond respectively to locations within axial power zone I and axial power zone V of Fig. 1.3.) The region inside the heating element is magnesium oxide (MGO), which electrically insulates the central thermocouple sheaths from the heating element.

The design difference between bundle 1 and bundle 2 is the thickness of the outer stainless steel sheath, which was increased from 0.254 mm to 0.381 mm. An idealized segment of a bundle 1 or bundle 2 fuel pin simulator is shown in Fig. 1.4, and the associated bundle 2 dimensions for axial power zones I and V are given in Table 1.1. The thermocouple bead (0.076 mm diam) is nominally centered 0.254 mm inside the outer surface of the inner sheath (0.635 mm from the pin surface) of a bundle 2 EFPS; therefore, that point is the radial position at which the EFPS temperature history is measured.

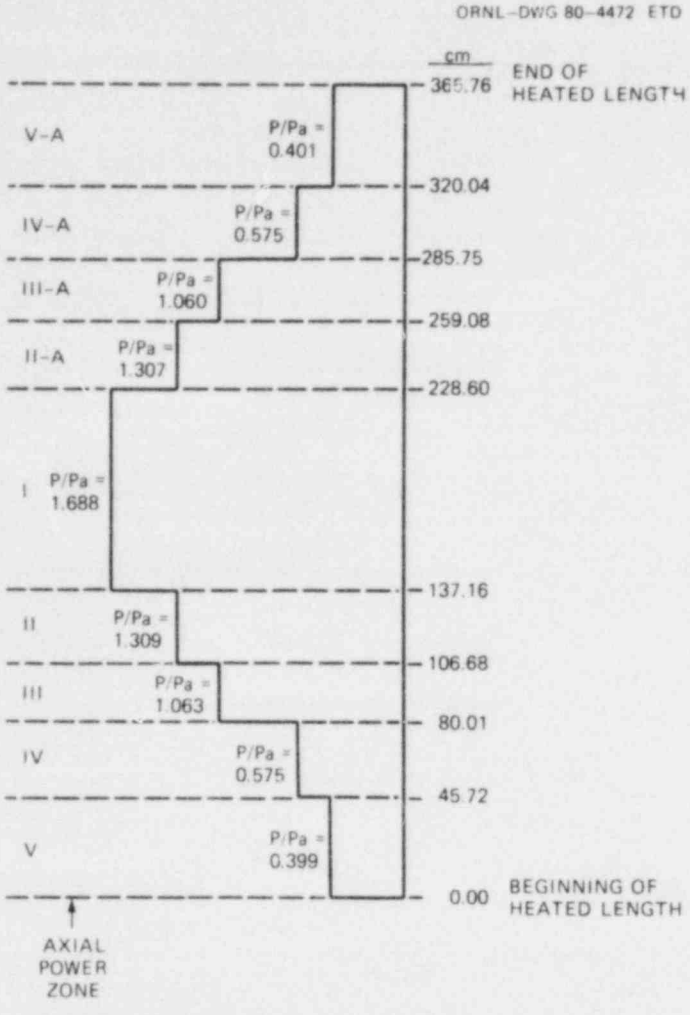

Fig. 1.3. Location of axial power zones and their local-to-average heat generation rates for bundle 1 or bundle 2 EFPS.

Table 1.1. Radial dimensions of bundle 2 EFPS at axial power zones I and V

Radial position[a]	Radial dimension (mm)	
	Axial power zone I	Axial power zone V
A	2.76	2.28
B	3.10	2.82
C	3.10	3.10
D	4.24	4.24
E	5.00	5.00
F	5.38	5.38

[a]The radial positions are referenced to Fig. 1.4.

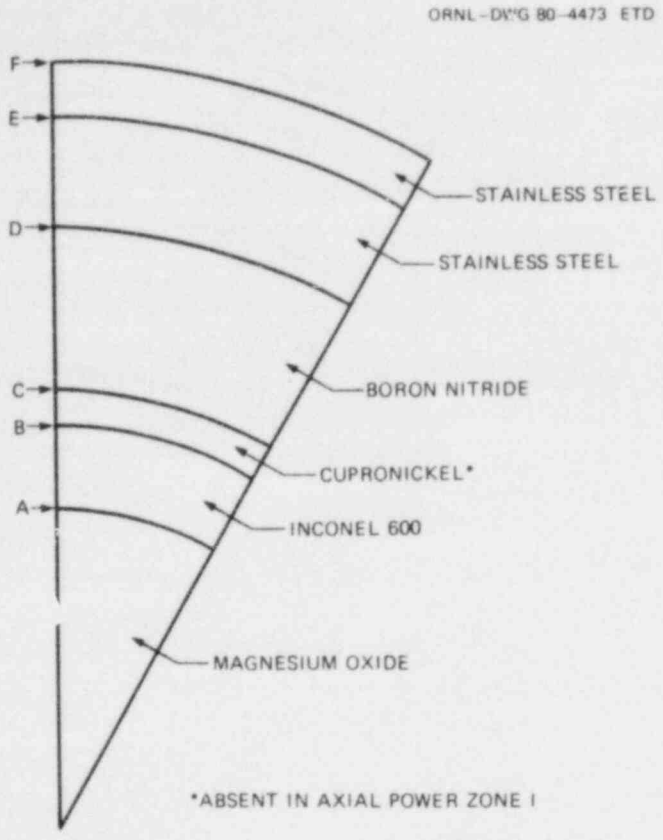

Fig. 1.4. Idealized EFPS segment construction details showing regional compositions and locations of the dimensions listed in Table 1.1.

2. REPORT OBJECTIVES

The physical location of the thermocouple bead (0.635 mm from the bundle 2 EFPS surface) affects its ability to record accurately the temperature transients occurring on the surface of the EFPS. For oscillatory surface phenomena, the recorded transient temperatures (i.e., thermocouple response) will be damped as compared with the surface temperatures and will exhibit some form of time response even if the EFPS is experiencing an extremely slow surface transient.

This investigation will determine the ability of thermocouples embedded at varying depths from the EFPS surface to represent accurately various frequency boundary conditions and will determine the time response associated with different thermocouple bead radial positions. A relationship will thus be established between the sheath thickness of the EFPS (because the thermocouple will be adjacent to the inner surface of this sheath) and the frequency range of surface phenomena that can be determined numerically with the internally measured temperature history as a boundary condition.

The procedure used to establish this relationship will be basically numeric. A one-dimensional model of a bundle 2 EFPS will be supplied to a forward-implicit version of ORINC,[2] which will be capable of using supplied steady-state and transient power generation rates and heat transfer coefficient–sink temperature combinations as boundary conditions; more specifically, a square-wave heat transfer coefficient of varying periods, a constant power generation rate, and a constant sink temperature will be used in the frequency response evaluation, whereas combinations of step drops, constant values, and step increases for the heat transfer coefficient, power generation rate, and sink temperature will be used in the time-response study.

The forward-implicit ORINC will be used to determine the internal transient temperature distribution resulting from these imposed boundary conditions. The calculated transient temperature at a given radial position will then be considered to be the signal of a thermocouple located at that radial position and experiencing the given boundary conditions.

3. THERMOCOUPLE FREQUENCY STUDY (TFS)

In loss-of-coolant accident experiments such as those performed at ORNL's THTF, high-speed data recording is extremely important because transient conditions such as 90 K surface temperature rises in 100 ms after departure from nucleate boiling and 200 K surface temperature drops in 200 ms during rewet are not uncommon. The THTF data acquisition system currently scans a given instrument at a rate of 20 times/s and thus can sense when these events occur. Because the thermocouple is embedded within the outer sheath of the EFPS, the question arises whether the thermocouple can be used to determine high-frequency transitory surface phenomena.

3.1 Forward-Implicit Version of ORINC

To answer the question of the resolving capability of the thermocouple and to influence the design of future EFPSs, a series of transient calculations was performed with a newly developed version of ORINC. This version has been modified to analyze data from the Forced Convection Test Facility (FCTF)[1] and to handle a maximum of 12 thermocouples, each of which is sampled 100 times/s.

In transforming ORINC to make it compatible with the FCTF, the overall calculational method, data input, code initialization, the code organization, and theory for solving transient, lumped-parameter formulation of the cylindrical (radially one-dimensional) heat conduction problem were preserved. Major changes involved converting the code to double precision; creating a variable timestep capability; implementing TRIDIG,[3] which is a tridiagonal matrix inversion subroutine; completely revising the output packages; and transforming the finite-differenced heat conduction equations from the inverse-implicit to the forward-implicit formulations with the power generation rate and the heat transfer coefficient-sink temperature combination as boundary conditions (each of which can be user-supplied for both steady-state and transient calculations). The boundary conditions are known at 10 ms intervals, so that for calculational timesteps < 10 ms ORINC cubically interpolates between the known values.

The bundle 2 ORINC pin model (Fig. 3.1) divides the EFPS into nodes numbered sequentially from the center of the EFPS and associates the internal temperatures with the calculated nodal centers of mass (COMs). The nodal interfaces (given by the solid lines in Fig. 3.1) and their corresponding COMs (given by the chain-dotted lines in Fig. 3.1) are determined by the number of nodes desired for each region and by the method of calculating the interface and center of mass radii documented in ORINC.[2]

For this study, there are six regions with nodes as follows: (1) four in the MGO core, (2) two in the Inconel 600 heater, (3) two in the cupronickel oversleeve (absent in axial power zone I), (4) three in the BN annulus, (5) three in the inner stainless steel sheath, and (6) two in the outer stainless steel sheath. The nodes—along with their inner and outer radii, COM radii, COM distances from the pin surface, regional materials, and regional thicknesses for axial power zones I and V—are given in Tables 3.1 and 3.2, respectively. The ORINC code is capable of modeling a gap between the inner and outer stainless steel sheaths; however, for this study it is set equal to zero, essentially creating one 1.143-mm-thick sheath.

The EFPS model does not physically incorporate the thermocouple but associates the center of the thermocouple bead with the nodal COM that most closely approximates its radial position; because the gap has been zeroed, the thermocouple bead can be associated with the radial position of any nodal COM. The region of interest, however, will be the stainless steel sheaths, which define an area within 1.143 mm of the surface of the EFPS.

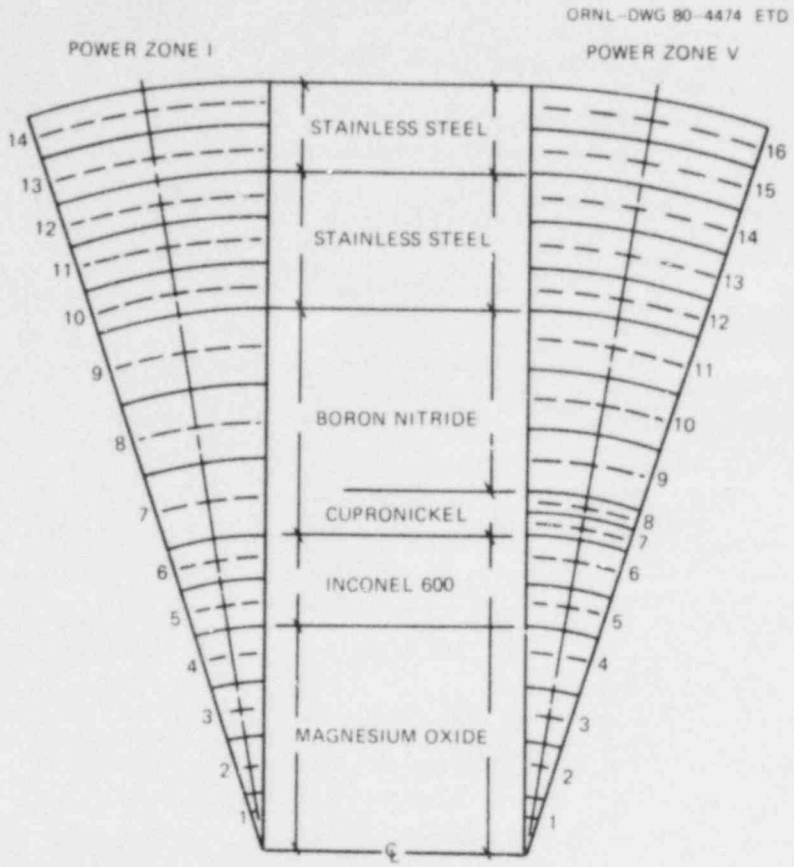

Fig. 3.1. ORINC model (one-dimensional along chain-dashed line) for a bundle 2 EFPS. Axial power zone V is represented by the 16-node model, and axial power zone I is represented by the 14-node model.

Table 3.1. Radial dimension information for ORINC model of bundle 2 EFPS at axial level corresponding to power zone I

Nodal identifier	Nodal inner radius (mm)	Nodal COM radius (mm)	Nodal outer radius (mm)	Nodal COM distance from surface (mm)	Nodal material composition	Material outer radius (mm)	Material thickness (mm)
℄	0.0	0.0	0.0	5.38	MGO	2.76	2.76
1	0.0	0.98	1.38	4.40	MGO	2.76	2.76
2	1.38	1.69	1.95	3.69	MGO	2.76	2.76
3	1.95	2.18	2.39	3.20	MGO	2.76	2.76
4	2.39	2.59	2.76	2.79	MGO	2.76	2.76
5	2.76	2.85	2.94	2.53	Inconel	3.10	0.34
6	2.94	3.02	3.10	2.36	Inconel	3.10	0.34
7	3.10	3.32	3.52	2.06	BN	4.24	1.14
8	3.52	3.71	3.90	1.67	BN	4.24	1.14
9	3.90	4.07	4.24	1.31	BN	4.24	1.14
10	4.24	4.38	4.51	1.00	Stainless steel	5.00	0.76
11	4.51	4.64	4.76	0.74	Stainless steel	5.00	0.76
12	4.76	4.89	5.00	0.49	Stainless steel	5.00	0.76
13	5.00	5.10	5.20	0.28	Stainless steel	5.38	0.38
14	5.20	5.29	5.38	0.09	Stainless steel	5.38	0.38
Surface	5.38	5.38	5.38	0.0	Stainless steel	5.38	0.38

Table 3.2. Radial dimension information for the ORINC model of bundle 2 EFPS at axial level corresponding to power zone V

Nodal identifier	Nodal inner radius (mm)	Nodal COM radius (mm)	Nodal outer radius (mm)	Nodal COM distance from surface (mm)	Nodal material composition	Material outer radius (mm)	Material thickness (mm)
℄	0.0	0.0	0.0	5.38	MGO	2.28	2.28
1	0.0	0.80	1.14	4.58	MGO	2.28	2.28
2	1.14	1.39	1.61	3.99	MGO	2.28	2.28
3	1.61	1.80	1.97	3.58	MGO	2.28	2.28
4	1.97	2.13	2.28	3.25	MGO	2.28	2.28
5	2.28	2.42	2.56	2.96	Inconel	2.82	0.54
6	2.56	2.69	2.82	2.69	Inconel	2.82	0.54
7	2.82	2.89	2.96	2.49	Cupronickel	3.10	0.28
8	2.96	3.03	3.10	2.35	Cupronickel	3.10	0.28
9	3.10	3.32	3.52	2.06	BN	4.24	1.14
10	3.52	3.71	3.90	1.67	BN	4.24	1.14
11	3.90	4.07	4.24	1.[illegible]	BN	4.24	1.14
12	4.24	4.38	4.51	1.00	Stainless steel	5.00	0.76
13	4.51	4.64	4.76	0.74	Stainless steel	5.00	0.76
14	4.76	4.89	5.00	0.49	Stainless steel	5.00	0.76
15	5.00	5.10	5.20	0.28	Stainless steel	5.38	0.38
16	5.20	5.29	5.38	0.09	Stainless steel	5.38	0.38
Surface	5.38	5.38	5.38	0.0	Stainless steel	5.38	0.38

3.2 Test Matrix Formulation

Seven transient cases were completed, each using the forward-implicit ORINC to calculate the internal temperature distributions using the previously discussed EFPS model, the supplied power generation rate, and the supplied heat transfer coefficient–sink temperature combination boundary conditions. Temperature histories were calculated for all nodal COMs, for the pin centerline, and for the pin surface at two axial levels, one located within axial power zone I and the other located within axial power zone V.

Identical steady-state boundary conditions were supplied for each case at each level, with the transient boundary conditions derived from their corresponding steady-state values, which are listed in Table 3.3. The power generation rates and the sink temperatures were held constant at their steady-state values for the duration of the transient. Thus, the only difference from one case to another involved the transient heat transfer coefficient, which was prescribed to be a square wave having a variable period and oscillating for ten cycles about the steady-state heat transfer coefficient from a minimum of 0.5 the steady-state value to a maximum of 1.5 the steady-state value. The seven cases were then defined by choosing seven periods for the square wave. The associated periods are tabulated in Table 3.4. The steady-state boundary condition combinations were chosen to allow power zone V to experience a steady-state forced-convection heat transfer mode and power zone I to experience a steady-state nucleate-boiling heat transfer mode.

Because the transient heat transfer coefficient boundary condition is composed of discrete data points, the number of these points that must be included in one cycle of the square wave must be determined if the function is to be represented accurately. The chosen value, 20, represents the number of calculational timesteps per square-wave cycle and creates the square wave pictured in Fig. 3.2. The 20 calculational timesteps per square-wave cycle, the 10-cycle square-wave duration, known square-wave

Table 3.3. Steady-state boundary conditions for all TFS cases

Boundary condition	Axial power zone I	Axial power zone V
Heat transfer coefficient, kW/(m^2·K)	69.105	12.473
Sink temperature, K	620.348	564.087
Local linear power generation rate, kW/m[a]	58.251	13.786

[a]Total rod power ~126 kW.

Table 3.4. TFS cases and their corresponding heat transfer coefficient square-wave periods

Case	Square-wave period (ms)
TFS1	1000
TFS2	200
TFS3	100
TFS4	50
TFS5	25
TFS6	10
TFS7	5

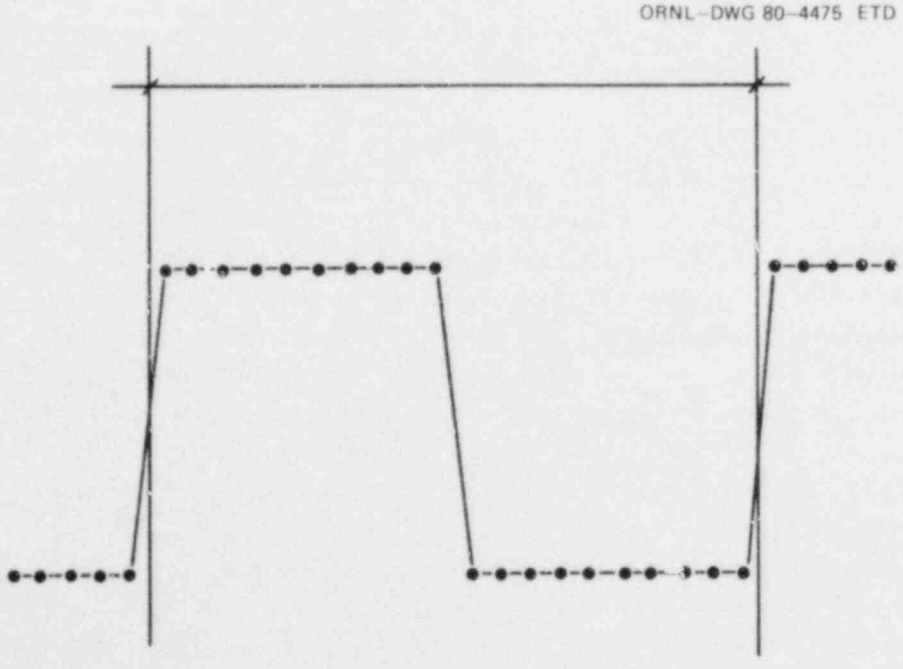

Fig. 3.2. Heat transfer coefficient square-wave boundary condition as constructed using 20 data points per cycle.

period, 5 periods of steady-state calculations preceding the square wave, and 15 periods of steady-state calculations following the square wave all combine to give unique definition to the 7 transients, which are listed with their transient length and calculational timestep information in Table 3.5. The heat transfer coefficient boundary conditions for axial power level V of cases TFS1, TFS4, and TFS7 are represented in Figs. 3.3 through 3.5. The heat transfer coefficient boundary conditions for the remaining cases are similarly constructed.

The EFPS interna' temperature histories, as calculated for the two power zones in each of the seven cases by the forward-implicit ORINC using these boundary conditions, can now be used to relate the depth of the thermocouple bead to its highest interpretable frequency and also to determine the maximum depth at which the thermocouple bead can be located and still resolve a particular surface condition frequency. The method of determining these relationships is first to associate the

Table 3.5. Calculational timestep and transient duration information for all TFS cases

Case	Square-wave period (ms)	Preceding steady state (ms)	Ten-cycle square wave (ms)	Following steady state (ms)	Total length of transient (ms)	Number of calculational timesteps in transient	Calculational timestep size (ms)
TFS1	1,000	5,000	10,000	15,000	30,000	600	50
TFS2	200	1,000	2,000	3,000	6,000	600	10
TFS3	100	500	1,000	1,500	3,000	600	5
TFS4	50	250	500	750	1,500	600	2.5
TFS5	20	100	200	300	600	600	1
TFS6	10	50	100	150	300	600	0.5
TFS7	5	25	50	75	150	600	0.25

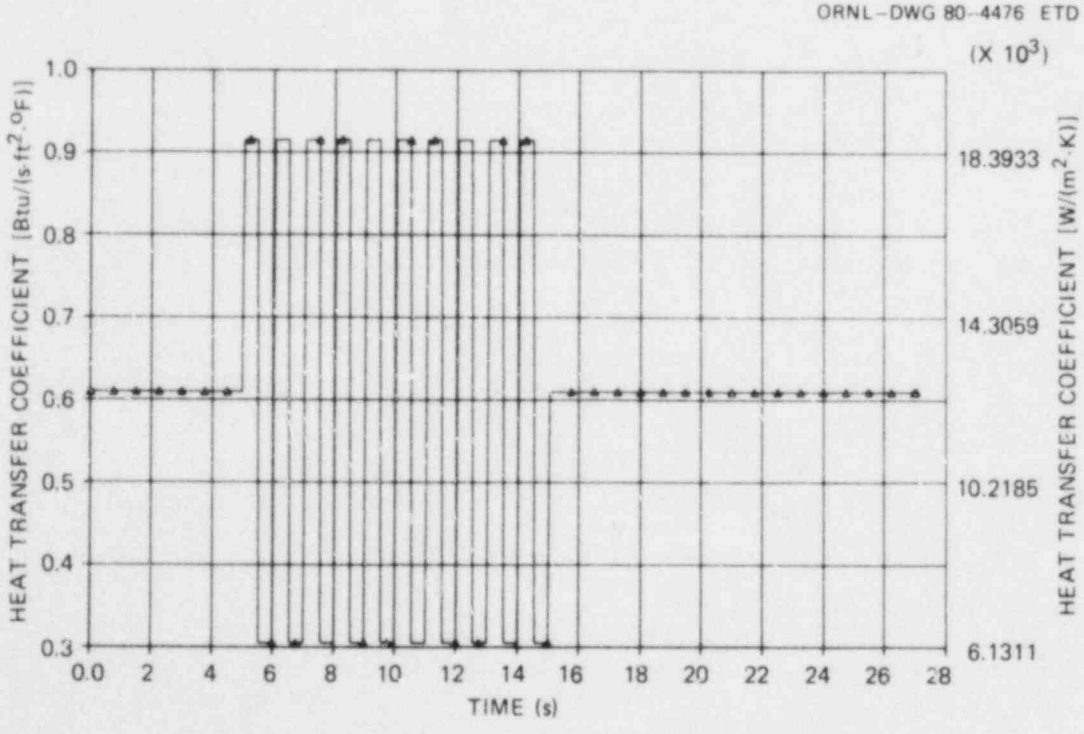

Fig. 3.3. Heat transfer coefficient boundary condition for case TFS1 involving axial power zone V.

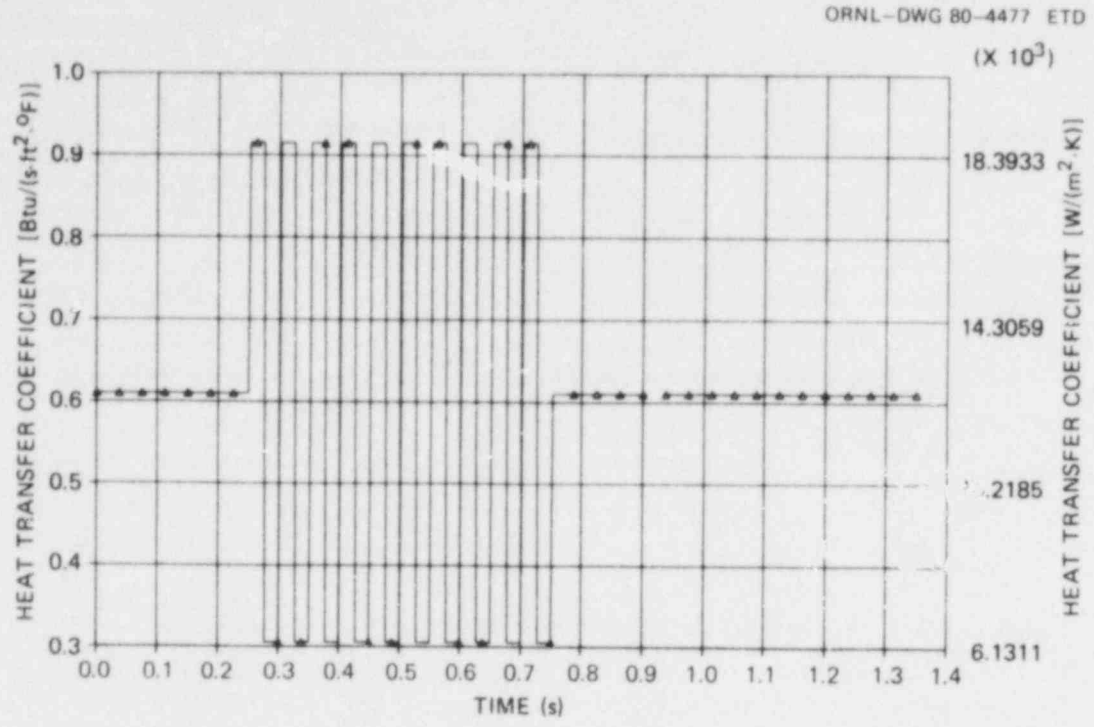

Fig. 3.4. Heat transfer coefficient boundary condition for case TFS4 involving axial power zone V.

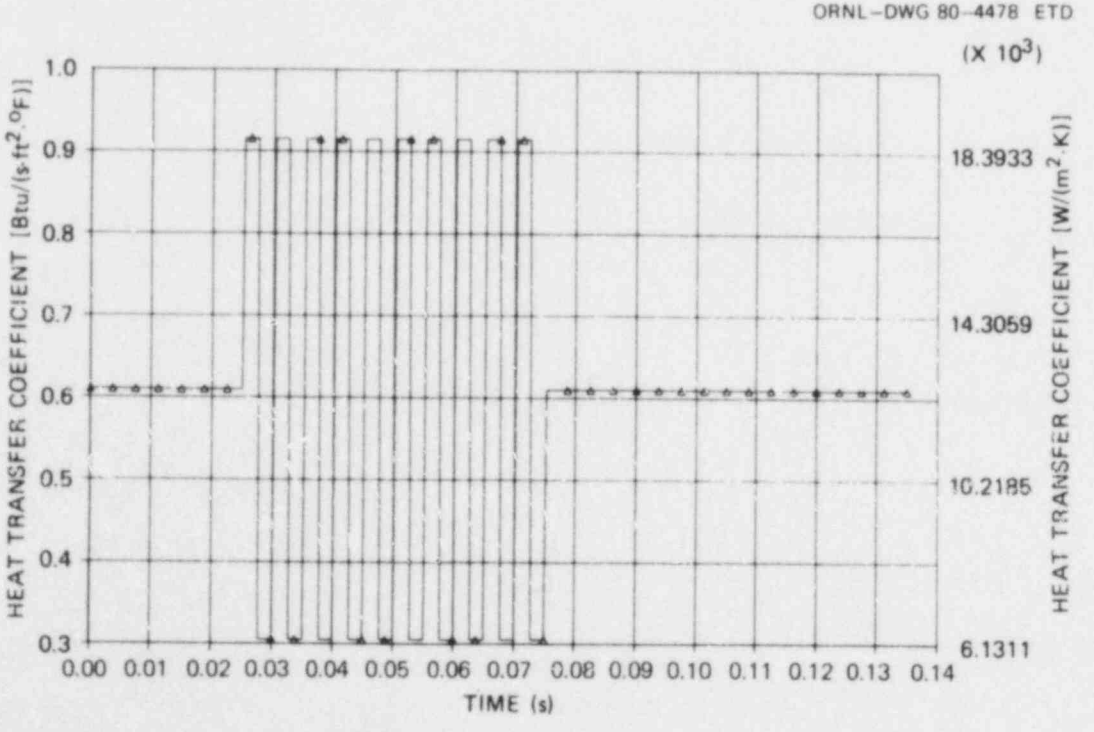

Fig. 3.5. Heat transfer coefficient boundary condition for case TFS7 involving axial power zone V.

thermocouple bea with a nodal COM and then to combine the temperature history for this nodal COM with the standard deviation of the thermocouple signal. This method yields an indication of the ability of the thermocouple to record the nodal COM temperature for a given frequency of surface phenomena; that is, the thermocouple may be able to record the nodal temperature history trace perfectly, but if the temperature oscillates (randomly or systematically) about a mean and if those oscillations are within $\pm 1\ \sigma$ (σ being the thermocouple signal standard deviation) of the mean, then those oscillations cannot be distinguished from the thermocouple signal uncertainty.

In applying this thermocouple frequency resolution analysis (Fig. 3.6), the mean oscillation amplitudes α are determined by locating a curve through the minimum cyclic temperatures and maximum cyclic temperatures occurring for the ten cycles. The nodal COM trend temperature, represented by the chain-dashed line in Fig. 3.6, is then found for a particular time by taking the average of the upper and lower mean oscillation amplitudes at that time.

Adding and subtracting the thermocouple signal standard deviation from the trend temperature curve results in the trend standard deviation curves, which are represented as the dashed lines in Fig. 3.6.

If the mean oscillation amplitude band 2α is greater than the trend standard deviation band 2σ, a thermocouple located at this nodal COM is considered capable of resolving the given frequency. Otherwise, the signal recorded by the thermocouple cannot adequately represent the nodal COM temperature, and as a result, the inverse-implicit ORINC will be unable to calculate the surface phenomena that actually occurred.

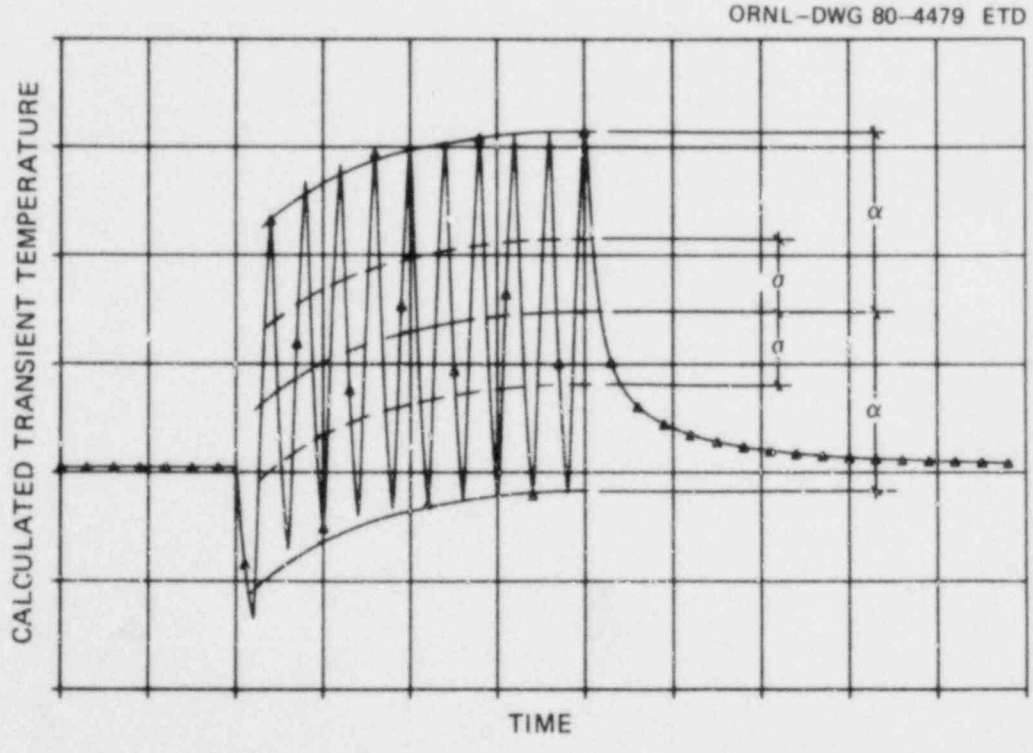

Fig. 3.6. Representation of thermocouple frequency resolution analysis incorporating the nodal COM trend temperature (- - -), the mean oscillation amplitude, α (——), and the trend standard deviation, σ (- - -) bands.

3.3 Period-Depth Correlation: Power Zone I

As seen in Table 3.1, the nodal COMs of most interest are those associated with nodes 10 through 14. The node 14 COM being so close to the surface (0.091 mm) will be omitted from the discussion because its response is indistinguishable from the surface response. Additionally, the calculated EFPS surface and EFPS centerline transient temperatures will be referenced; the calculated EFPS surface heat flux will be presented for comparative purposes.

The standard deviation on the thermocouples used in the THTF EFPSs, as given by the manufacturer,[1] is 2.389 K, a value consisting of both a systematic and a random component. In applying the thermocouple signal uncertainty to an oscillatory phenomenon, the random contribution to this uncertainty effectively represents the total uncertainty, for the systematic term produces only a relative shift in the thermocouple signal. For this study, a more appropriate estimate of the thermocouple signal standard deviation can therefore be obtained by determining the magnitude of the random uncertainty through examination of actual steady-state thermocouple signals. The maximum standard deviation of the steady-state thermocouple signal for all thermocouples located in axial power zone I was found to be roughly 0.233 K. As a conservative figure, a standard deviation of 0.556 K is used for the thermocouple signal. This value, combined with the results obtained in the TFS case studies for axial power zone I, was interpreted by using the previously discussed method to yield Table 3.6.

For example, the node 10 through 13 COM temperatures for case TFS1 (1000 ms step-wave period and axial power zone I) are presented in Figs. 3.7 through 3.10. From these figures it is evident that a thermocouple located at any of these radial positions can accurately represent a surface phenomenon having a period of 1000 ms. Also, α/σ decreases as the radial position approaches the center of the EFPS. The radial position where $\alpha/\sigma = 1.0$ would be the maximum depth at which a thermocouple bead could be located and still resolve the surface phenomenon occurring at the given period.

Figure 3.11 represents the calculated EFPS centerline temperature for case TFS1 and axial power zone I. The quantity α/σ is less than 1.0; thus the centerline cannot distinguish surface phenomena having a period of 1000 ms. Because $\alpha/\sigma < 1.0$ at this point, the maximum thermocouple bead depth at which the surface phenomenon can be resolved occurs between the radial position of the node 10 COM and the EFPS centerline. The calculated surface temperature and surface heat flux for case TFS1 and axial power zone I are presented in Figs. 3.12 and 3.13.

Table 3.6. Thermocouple frequency resolution analysis results for axial power zone I

Case	€	Nodal COM				Surface
		10	11	12	13	
TFS1		a	a	a	a	a
TFS2		a	a	a	a	a
TFS3			a	a	a	a
TFS4				a	a	a
TFS5					a	a
TFS6						a
TFS7						a

[a]Thermocouple bead located at this radial position can resolve temperature oscillations at the given frequency.

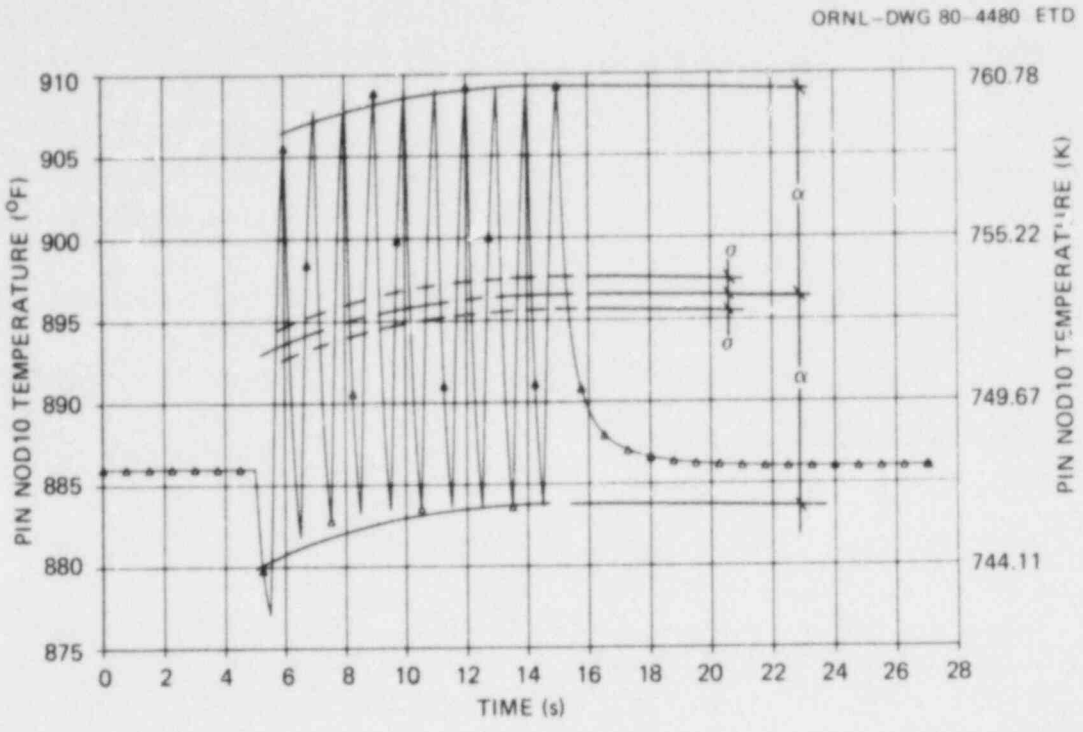

Fig. 3.7. NOD10 COM temperature and its associated mean oscillation amplitude and trend standard deviation bands. Calculations correspond to case TFS1 and axial power zone I.

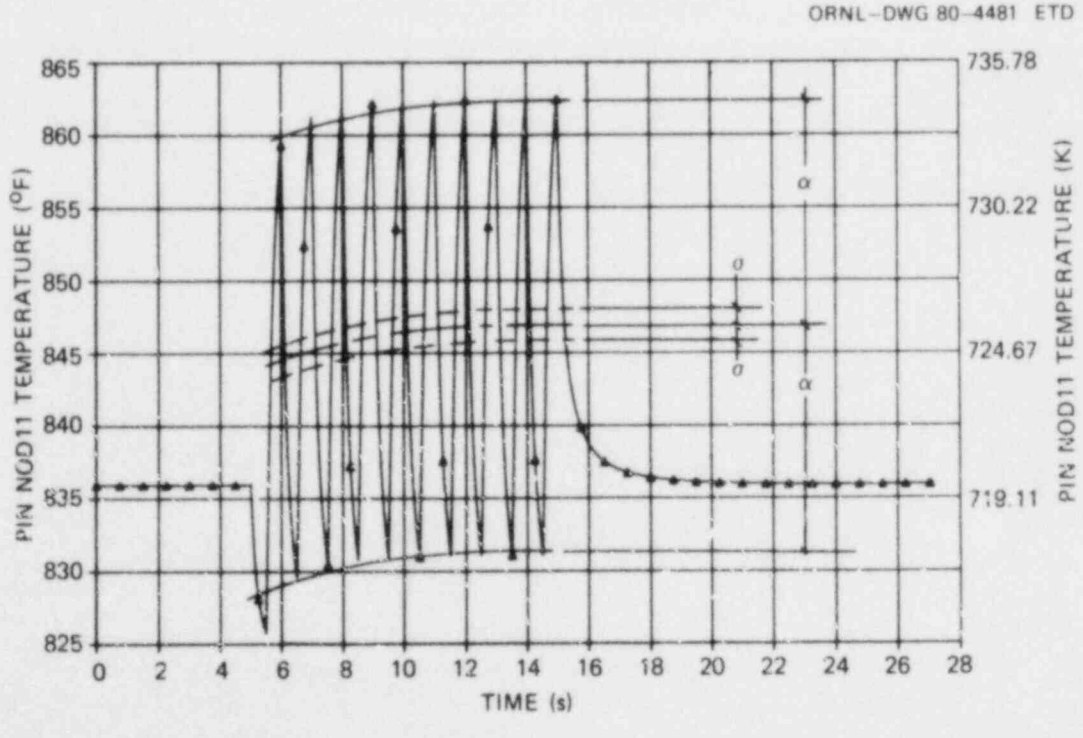

Fig. 3.8. NOD11 COM temperature and its associated mean oscillation amplitude and trend standard deviation bands. Calculations correspond to case TFS1 and axial power zone I.

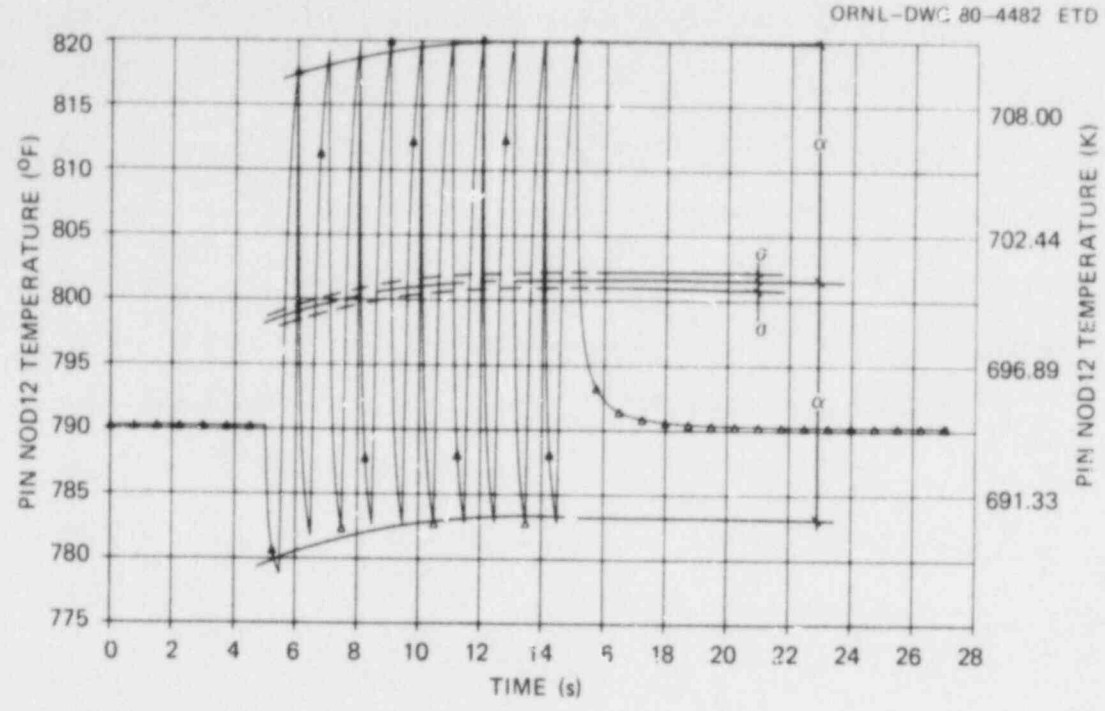

Fig. 3.9. NOD12 COM temperature and its associated mean oscillation amplitude and trend standard deviation bands. Calculations correspond to case TFS1 and axial power zone I.

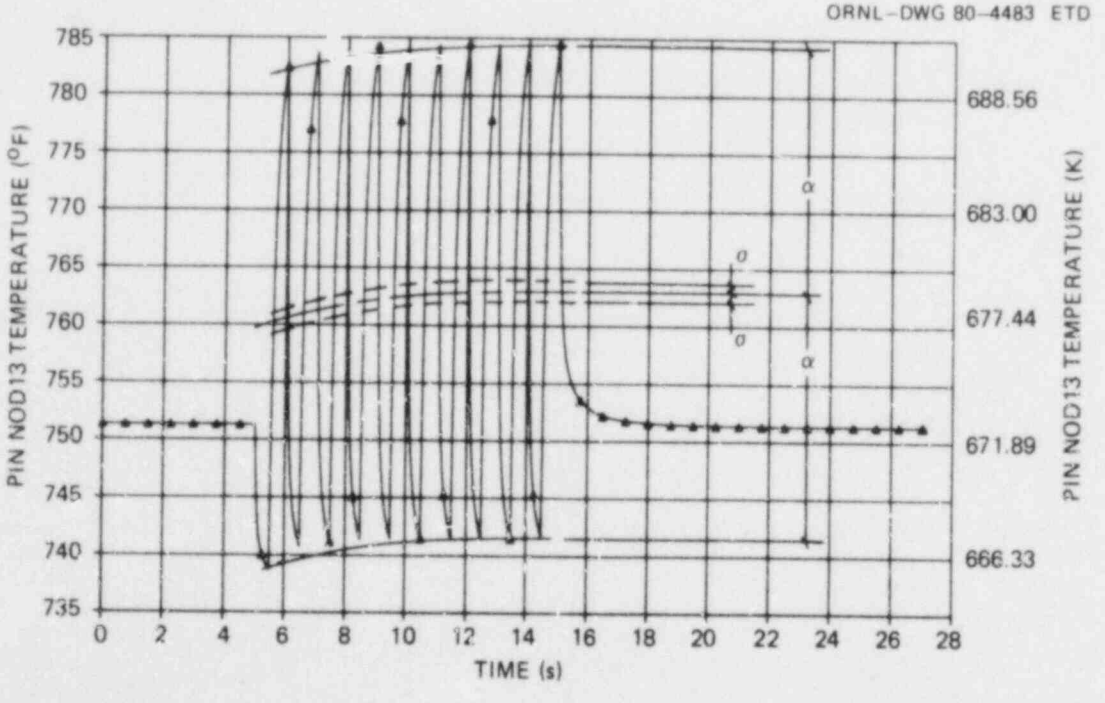

Fig. 3.10. NOD13 COM temperature and its associated mean oscillation amplitude and trend standard deviation bands. Calculations correspond to case TFS1 and axial power zone I.

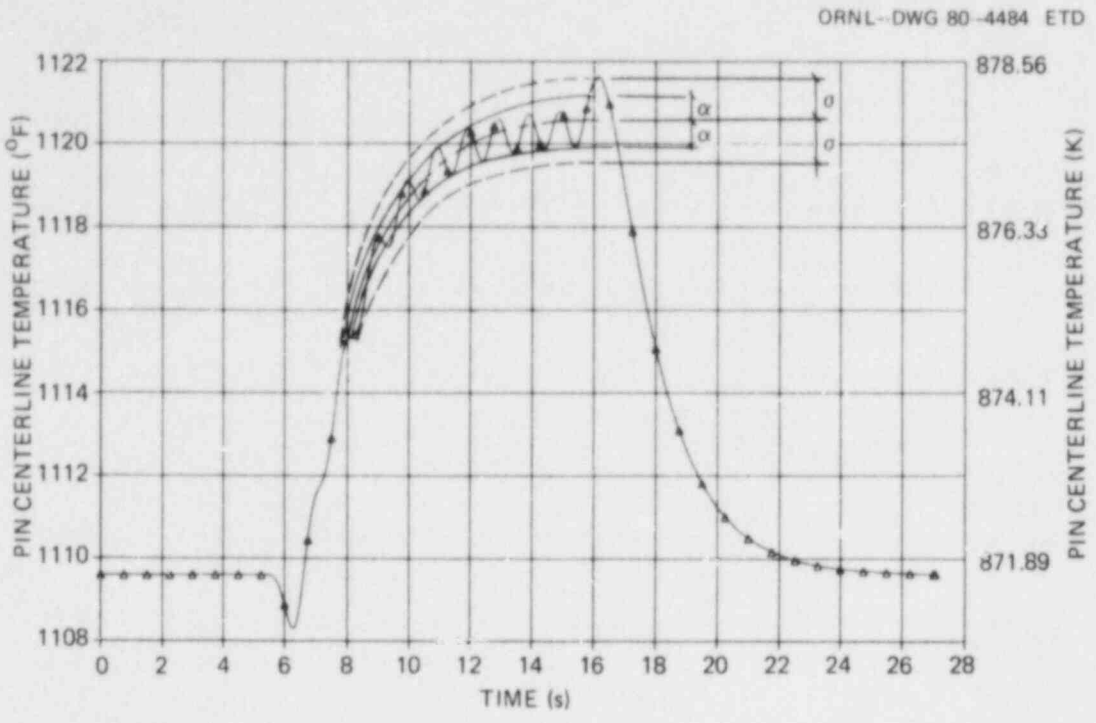

Fig. 3.11. EFPS centerline temperature and its associated mean oscillation amplitude and trend standard deviation bands. Calculations correspond to case TFS1 and axial power zone I.

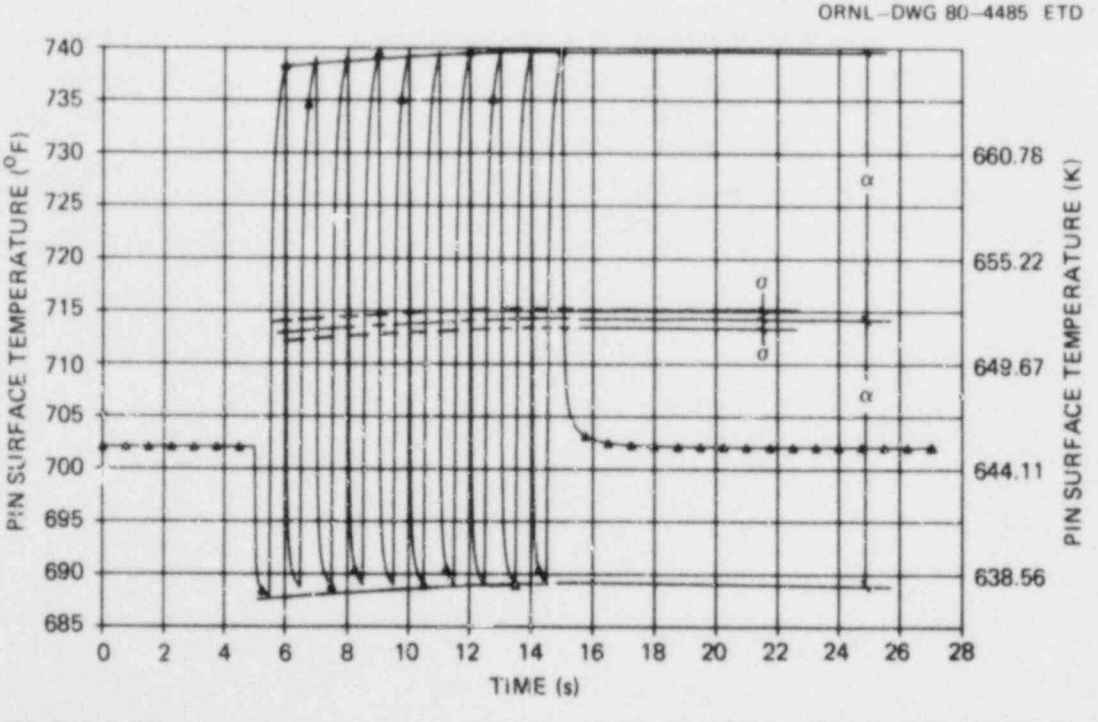

Fig. 3.12. EFPS surface temperature and its associated mean oscillation amplitude and trend standard deviation bands. Calculations correspond to case TFS1 and axial power zone I.

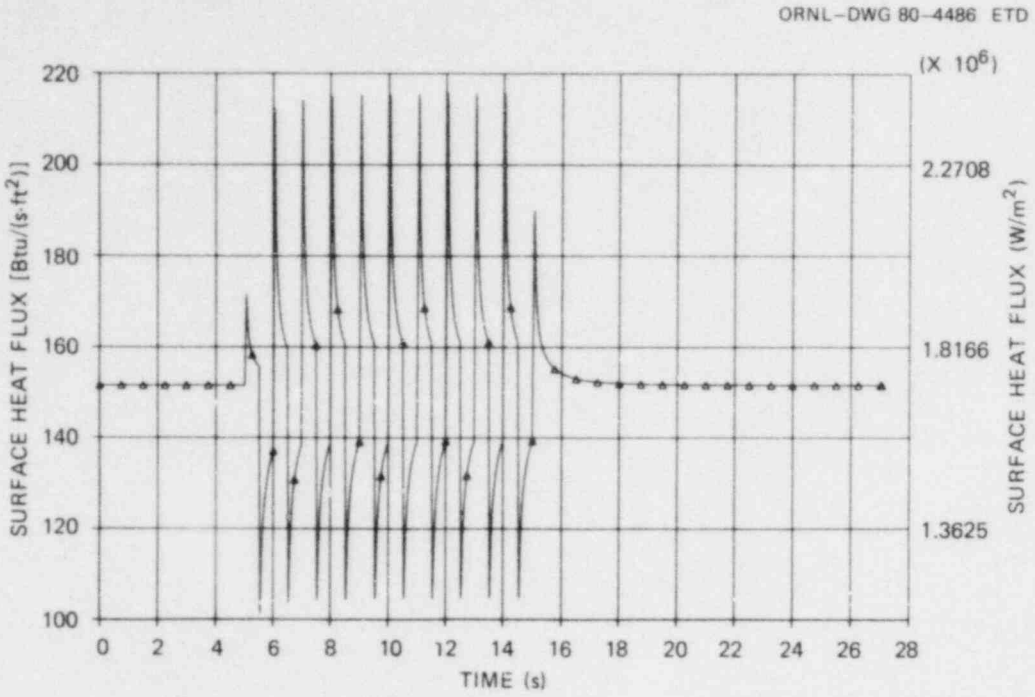

Fig. 3.13. Calculated EFPS surface heat flux corresponding to case TFS1 and axial power zone I.

3.4 Period-Depth Correlation: Power Zone V

In Table 3.2, the nodal COMs of most interest are those associated with nodes 12 through 16. The node 16 COM will be omitted from the discussion because it is indistinguishable from the surface response. The calculated EFPS centerline and EFPS surface transient temperatures will also be analyzed; the calculated EFPS surface heat flux will be presented for comparative purposes.

The thermocouple standard deviation is combined with the calculational results obtained in the TFS case studies for axial power zone V and subjected to the thermocouple frequency response analysis to produce Table 3.7. Because the analysis is identical to that performed for axial power zone I, no further discussion of the procedure is needed at this point.

Table 3.7. Thermocouple frequency resolution analysis results for axial power zone V

Case	€	Nodal COM				Surface
		12	13	14	15	
TFS1		a	a	a	a	a
TFS2			a	a	a	a
TFS3				a	a	a
TFS4					a	a
TFS5						a
TFS6						a
TFS7						a

[a]Thermocouple bead located at this radial position can resolve temperature oscillations at the given frequency.

3.5 Period-Depth Composite Relationship

The period-depth results summarized in Tables 3.6 and 3.7 indicate dual areas in the two-dimensional space defined by the thermocouple bead distance from the EFPS surface and by the period of the phenomena occurring on the EFPS surface. The first area represents the combinations of thermocouple bead depths and surface phenomena periods that yield thermocouple signals which, when supplied to the inverse-implicit ORINC can accurately reproduce the EFPS surface conditions. The remaining area in this two-dimensional space represents the thermocouple bead depths that provide thermocouple signals incapable of resolving the given frequency of surface oscillation.

These areas, as determined for axial power zone I, are shown in Fig. 3.14 with the crosshatched portion representing the desirable combinations. Figure 3.15 presents the areas as determined for axial power zone V, with the crosshatched portion again representing the desirable combinations.

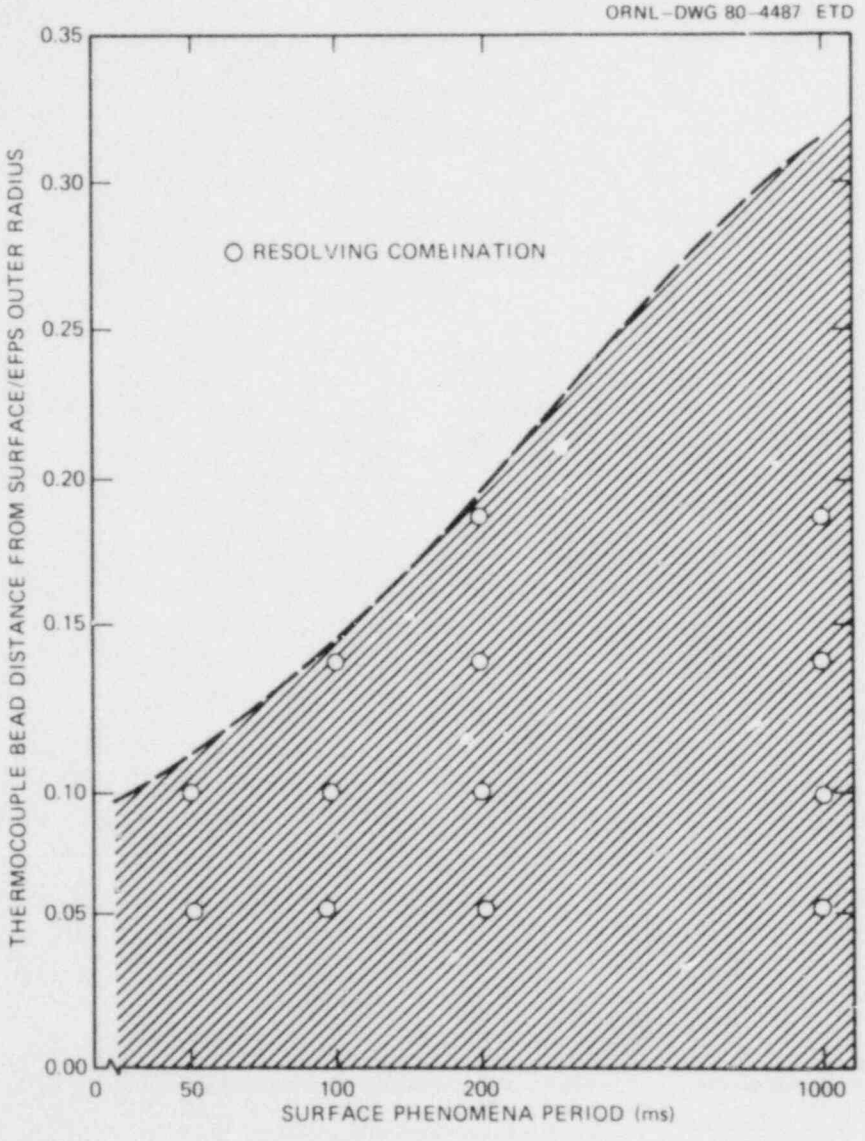

Fig. 3.14. Desirable combinations (represented by crosshatched area) of thermocouple bead depth and surface phenomenon period as determined by cases TFS1 through TFS7 involving axial power zone I.

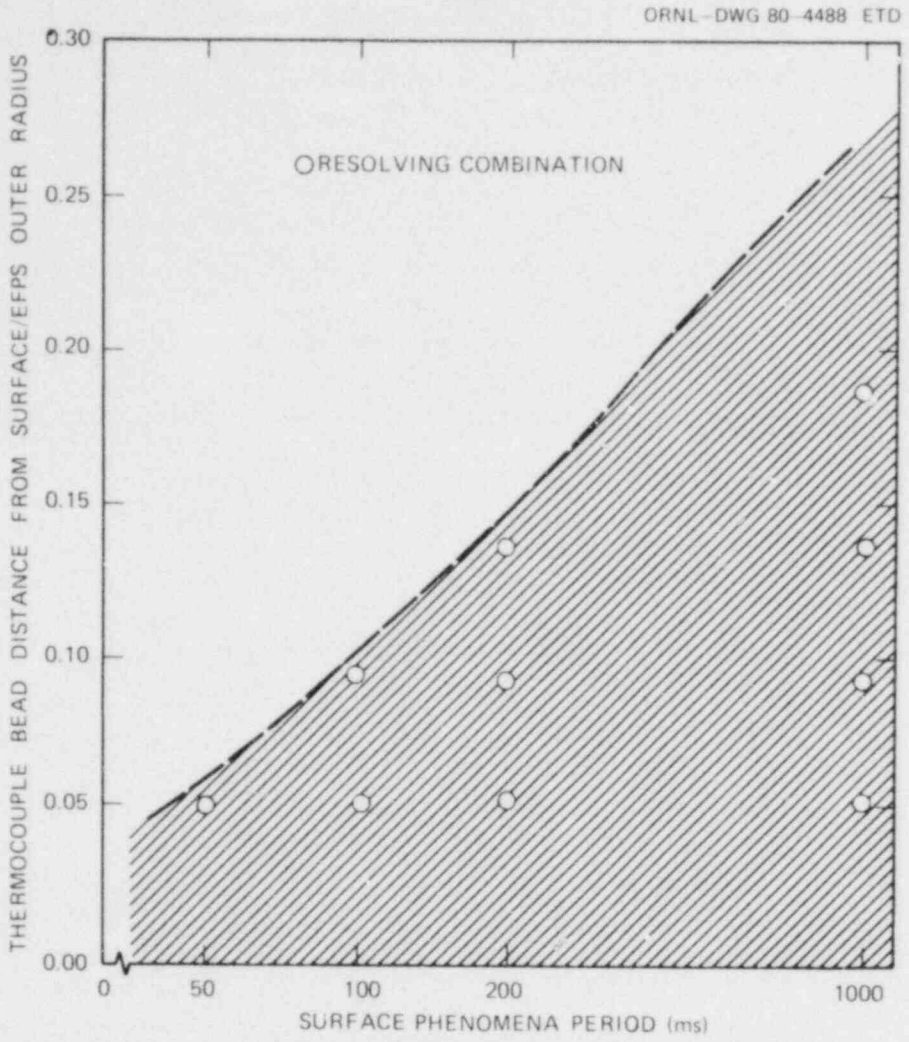

Fig. 3.15. Desirable combinations (represented by crosshatched area) of thermocouple bead depth and surface phenomenon period as determined by cases TFS1 through TFS7 involving axial power zone V.

The effect of the power generation rate and the heat transfer mode on the number of desirable combinations can be seen from the larger area in Fig. 3.14 as compared with Fig. 3.15. This increase in desirable combinations is due to the larger magnitude of the nodal COM temperature oscillations in the region of axial power zone I; these oscillations correspond to a larger surface temperature oscillation that will propagate further into the EFPS, thus increasing the depth at which the thermocouple bead can resolve the given frequency.

4. THERMOCOUPLE RESPONSE STUDY (TRS)

In addition to the damping of the node COM temperatures near the center of the EFPS, a companion physical situation affects the ability of the thermocouple to record surface phenomena accurately. This situation, which can be associated with various radial positions, is the time response; it is often described in terms of a time constant, is characterized by the capacity of a system to store energy, and is measured by the time necessary for a system or one of its components to adjust to an external input.

To determine how an indirectly heated EFPS responds to a sudden change in surface conditions, a series of transient calculations was performed using the forward-implicit version of ORINC, as described in Chap. 3. A bundle 2 ORINC EFPS model (Fig. 3.1) identical to that used in the thermocouple position frequency sensitivity study was supplied; because the EFPS models are identical, the geometry specified in Tables 3.1 and 3.2 remains valid.

A gap of ~0.0254 mm is included between the inner and outer stainless steel sheaths in this study. It is incorporated in the ORINC formulation as a heat transfer resistance term and therefore does not change the geometry of the EFPS model. The gap is important in the TRS because the behavior of bundle 1 and bundle 2 EFPSs is being examined, whereas in the TFS, the gap was omitted because the primary purpose was support for the design of bundle 3* EFPSs. The omission of the gap thus allowed effective transformation of the ORINC EFPS from a bundle 2 design—with an outer sheath thickness of 0.381 mm, an inner sheath thickness of 0.762 mm, and a gap[4] between these sheaths—into a bundle 3 design—with a single outer sheath 1.143 mm thick.

4.1 Test Matrix Formulation

Thirty cases, each involving 3000 transient timesteps, were studied with the forward-implicit ORINC calculating the internal temperature distributions using the power generation rate and the heat transfer coefficient–sink temperature combination as boundary conditions. Temperature histories were generated for (1) all nodal COMs, (2) the EFPS centerline, and (3) the EFPS surface for an axial level located within either power zone I or power zone V (Fig. 1.3). The EFPS transient surface heat flux was also determined by ORINC for each case.

These 30 cases can be arranged into 1 major group and 4 comparative groups. The major group consists of 22 cases, with calculations corresponding to an EFPS geometry at an axial level within power zone V, where the EFPS is subjected to a sufficient steady-state power generation rate to necessitate an initial temperature profile to be considerably higher than the sink temperature. At the initiation of the transient, the power generation rate is reduced to zero; the rod then cools until it attains equilibrium with the sink temperature, which is held constant at its steady-state value over the duration of the transient. The heat transfer coefficient is stepped at the time of the drop in the power generation rate, with the size of the step increase defining the different surface conditions to which the EFPS can respond. The 22 cases in the major group, which are distinguished by the calculational timestep size and by the magnitude of the step of the heat transfer coefficient boundary condition, are known as TRS01 through TRS22.

The first comparative group experiences the same type of transient as the major group, with calculations being performed for an EFPS geometry at an axial level within power zone I. In the first comparative group the cases are known as TRS23 and TRS24.

---

*Bundle 3 refers to the third EFPS bundle (8 × 8 array) designed for testing in the THTF.

The second and third comparative groups, for which calculations are performed for EFPS geometries at axial levels corresponding to power zones V and I, respectively, consist of two cases each in which the power generation rate is zero over the duration of the transient, and the sink temperature and heat transfer coefficient are stepped at the beginning of the transient. Because the power generation rate equals zero at all times, the EFPS is initially at equilibrium with the sink temperature and must again attain this equilibrium with the sink temperature when the sink temperature is step-increased. The heat transfer coefficient is stepped at the time corresponding to the step in the sink temperature; the size of the step increase distinguishes the two cases in each group and defines different surface conditions to which the EFPS can respond. The cases composing the second and third comparative groups are known as TRS25, TRS26, TRS27, and TRS28, respectively.

In the fourth comparative group are two cases that have (1) steady-state boundary conditions similar to those used in the TFS and (2) correspond to the EFPS geometries of axial power zones V and I, respectively. These cases, TRS29 and TRS30, experience a transient consisting of a constant sink temperature, a constant power generation rate, and a step-decreased heat transfer coefficient.

Calculational timestep size, steady-state boundary conditions, and transient boundary conditions for the TRS cases TRS01 through TRS30 are listed in Tables 4.1 and 4.2.

Table 4.1. Steady-state (t = 0) boundary conditions and calculational timestep size for all TRS cases

TRS case	Calculational timestep (ms)	Local linear power generation rate (kW/m)[a]	Sink temperature (K)	Heat transfer coefficient [kW/(m^2·K)]
1	10.0	(3.2808) (0.39971)	299.66	0.1703
2	10.0	(3.2808) (0.39971)	299.66	0.1703
3	10.0	(3.2808) (0.39971)	299.66	0.1703
4	10.0	(3.2808) (0.39971)	299.66	0.1703
5	10.0	(3.2808) (0.39971)	299.66	0.1703
6	10.0	(3.2808) (0.39971)	299.66	0.1703
7	10.0	(3.2808) (0.39971)	299.66	0.1703
8	10.0	(3.2808) (0.39971)	299.66	0.1703
9	10.0	(3.2808) (0.39971)	299.66	0.1703
10	10.0	(3.2808) (0.39971)	299.66	0.1703
11	10.0	(3.2808) (0.39971)	299.66	0.1703
12	10.0	(3.2808) (0.39971)	299.66	0.1703
13	10.0	(3.2808) (0.39971)	299.66	0.1703
14	0.10	(3.2808) (0.39971)	299.66	0.1703
15	0.10	(3.2808) (0.39971)	299.66	0.1703
16	0.10	(3.2808) (0.39971)	299.66	0.1703
17	0.10	(3.2808) (0.39971)	299.66	0.1703
18	0.10	(3.2808) (0.39971)	299.66	0.1703
19	0.10	(3.2808) (0.39971)	299.66	0.1703
20	0.10	(3.2808) (0.39971)	299.66	0.1703
21	0.10	(3.2808) (0.39971)	299.66	0.1703
22	0.10	(3.2808) (0.39971)	299.66	0.1703
23	10.0	(3.2808) (1.68893)	299.66	0.1703
24	10.0	(3.2808) (1.68893)	299.66	0.1703
25	10.0	0.0	299.66	0.1703
26	10.0	0.0	299.66	0.1703
27	10.0	0.0	299.66	0.1703
28	10.0	0.0	299.66	0.1703
29	10.0	(34.4894) (0.39971)	564.08	15.0481
30	10.0	(34.4894) (1.68893)	620.35	187.9464

[a]0.39971 and 1.68893 are the axial peaking factors for power zones V and I, respectively.

Table 4.2. Transient ($0 < t \leq t_{end}$) boundary conditions and calculational timestep size for all TRS cases

TRS case	Calculational timestep (ms)	Local linear power generation rate (kW/m)[a]	Sink temperature (K)	Heat transfer coefficient [kW/(m²·K)]
1	10.0	0.0	299.66	0.5677
2	10.0	0.0	299.66	1.1354
3	10.0	0.0	299.66	1.7030
4	10.0	0.0	299.66	2.8384
5	10.0	0.0	299.66	3.9738
6	10.8	0.0	299.66	5.6768
7	10.0	0.0	299.66	8.5152
8	10.0	0.0	299.66	11.3536
9	10.0	0.0	299.66	17.0304
10	10.0	0.0	299.66	22.7072
11	10.0	0.0	299.66	28.3840
12	10.0	0.0	299.66	34.0608
13	10.0	0.0	299.66	170.3040
14	0.10	0.0	299.66	17.0304
15	0.10	0.0	299.66	22.7072
16	0.10	0.0	299.66	28.3840
17	0.10	0.0	299.66	34.0608
18	0.10	0.0	299.66	39.7376
19	0.10	0.0	299.66	56.7680
20	0.10	0.0	299.66	113.5360
21	0.10	0.0	299.66	170.3040
22	0.10	0.0	299.66	227.0720
23	10.0	0.0	299.66	1.7030
24	10.0	0.0	299.66	17.0304
25	10.0	0.0	373.00	1.7030
26	10.0	0.0	373.00	17.0304
27	10.0	0.0	373.00	1.7030
28	10.0	0.0	373.00	17.0304
29	10.0	(34.4894) (0.39971)	564.08	1.5048
30	10.0	(34.4894) (1.68893)	620.35	18.7946

[a]0.39971 and 1.68893 are the axial peaking factors for power zones V and I, respectively.

The EFPS internal temperature histories as calculated by the forward-implicit ORINC using the tabulated boundary conditions can now be used to relate the depth of the thermocouple bead to a time constant associated with the radial location of the thermocouple. If the thermocouple is assumed to reside at a given nodal COM that nodal COM transient temperature is used to yield a radially dependent time constant directly related to the phenomena on the surface.

4.2 Radial Time Constant Determination

A widely accepted model for system dynamic response[5] is the ordinary differential equation with constant coefficients:

$$a_n \frac{d^n x_{out}}{dt^n} + a_{n-1} \frac{d^{n-1} x_{out}}{dt^{n-1}} + \ldots + a_1 \frac{dx_{out}}{dt} + a_0 x_{out} =$$

$$b_m \frac{d^m x_{in}}{dt^m} + b_{m-1} \frac{d^{m-1} x_{in}}{dt^{m-1}} + \ldots + b_1 \frac{dx_{in}}{dt} + b_0 x_{in} , \qquad (4.1)$$

where

a_i = constants, i = 0, 1, ..., n;

b_j = constants, j = 0, 1, ..., m;

t = time;

x_{out} = system response quantity;

x_{in} = system input quantity.

If the EFPS is assumed to be a first-order system, a complete solution to Eq. (4.1) (relative to the initial system temperatures and forced by a step in the input system temperature occurring at t = 0) of the following form can be obtained:

$$T(r, t) = T(r, 0) + [T(r, \infty) - T(r, 0)][1.0 - e^{-t/\tau(r)}], \tag{4.2}$$

where

T(r, t) = temperature at radial position r and time t = t,

T(r, 0) = temperature at radial position r and time t = 0,

T(r, ∞) = temperature at radial position r and time t = ∞,

$\tau(r)$ = EFPS time constant at radial position r.

The complete transformation from Eq. (4.1) to Eq. (4.2) can be found in Appendix A.

Substituting $t = \tau(r)$ into Eq. (4.2) results in

$$T[r, \tau(r)] = T(r, 0) + [T(r, \infty) - T(r, 0)][1.0 - e^{-1.0}] \tag{4.3}$$

or

$$T[r, \tau(r)] = T(r, 0) + [T(r, \infty) - T(r, 0)][0.63212]. \tag{4.4}$$

Equation (4.4) is valid for all TRS cases [i.e., T(r, ∞) can be higher than T(r, 0) or T(r, ∞) can be lower than T(r, 0)] because Eq. (4.4) is dependent on both the sign and the magnitude of the difference in T(r,∞) and T(r, 0). This is shown by Fig. 4.1 and 4.2, which graphically portray the relationship between $\tau(r)$ and [T(r, ∞) − T(r, 0)] for a cooling case and a heating case, respectively.

Because the nodal COMs, EFPS centerline, and EFPS surface transient temperature histories have been generated for each TRS case by the forward-implicit ORINC, the temperature $T[r_0, \tau(r_0)]$ for a particular radial position r_0, corresponding to the time $t = \tau(r_0)$, can be calculated from Eq. 4.4 using the steady-state temperature $T(r_0, 0)$ and the final equilibrium temperature $T(r_0, \infty)$. The value of the radially dependent time constant $\tau(r_0)$ is determined by using this known temperature $T[r_0, \tau(r_0)]$, the ORINC-calculated temperature-time table, and the method illustrated in Fig. 4.1 or 4.2. Thus, the ORINC-calculated transient temperature profiles are scanned at the radial position r_0 until $T[r_0, \tau(r_0)]$ lies between two successive timestep temperatures. The time of the first of these two temperature profiles is assumed to be $\tau(r_0)$; therefore, the error in $\tau(r_0)$ is less than the calculational timestep size for that particular case because $T[r_0, \tau(r_0)]$ is guaranteed to occur before the time of the second temperature profile.

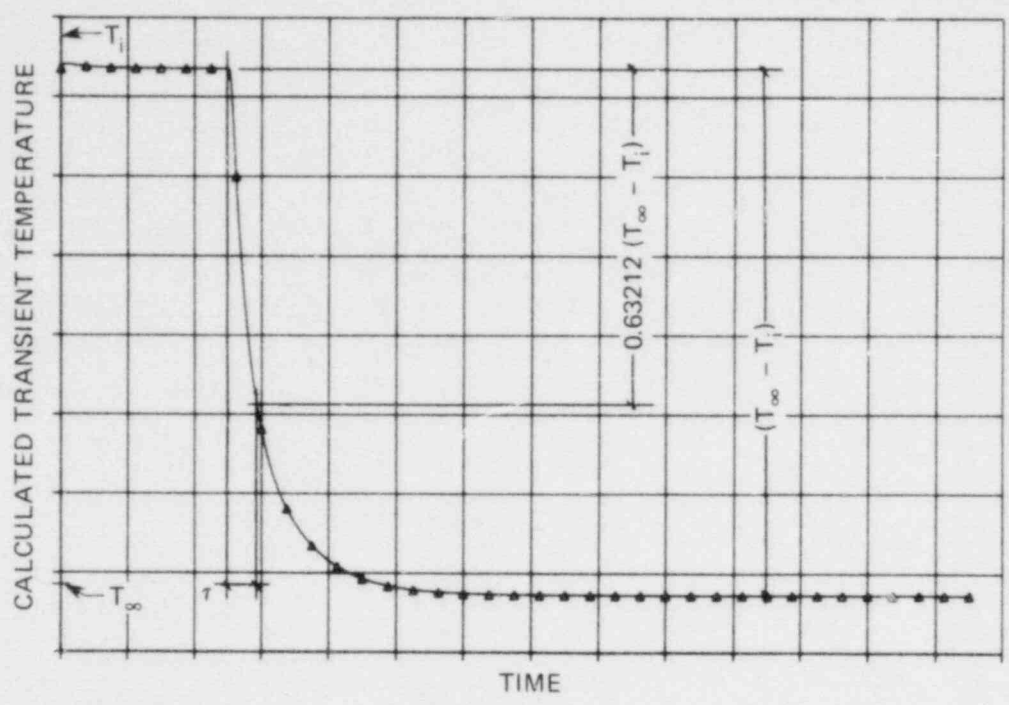

Fig. 4.1. First-order time-response relationship between τ and $(T_\infty - T_i)$ for $T_\infty < T_i$ at a given radial position.

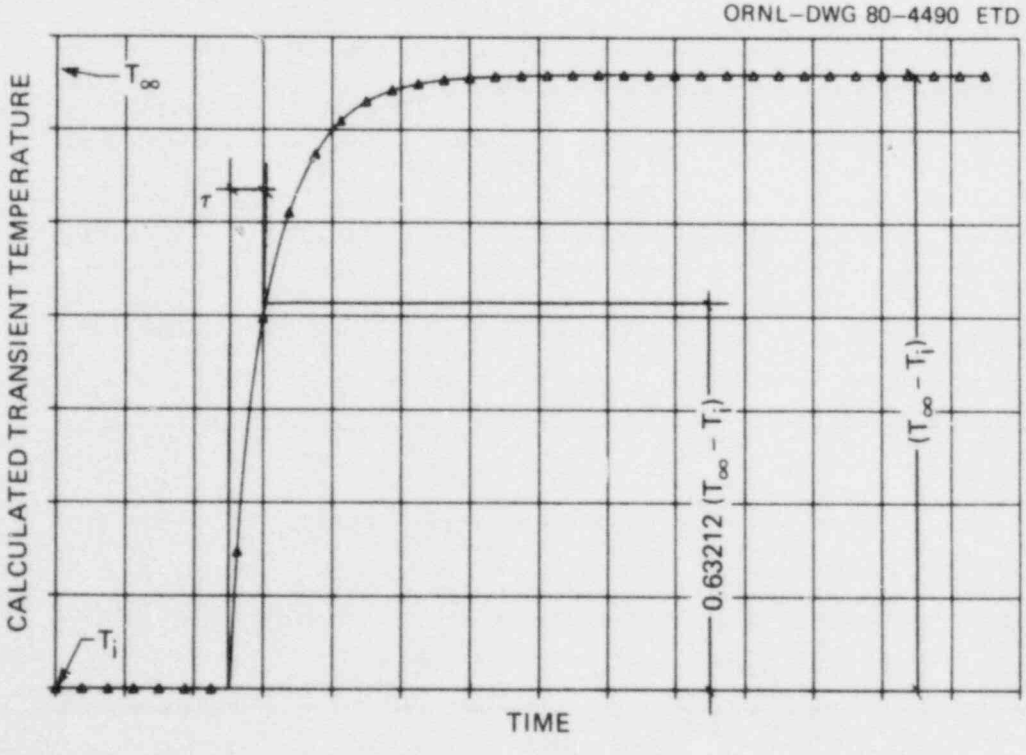

Fig. 4.2. First-order time-response relationship between τ and $(T_\infty - T_i)$ for $T_\infty > T_i$ at a given radial position.

As seen in Tables 3.1 and 3.2, the nodal COMs of most interest are those associated with the five outer nodes of either geometry. The outermost node (14 for axial power zone I and 16 for axial power zone V) will be omitted from the discussion since they are indistinguishable from the surface response. The ORINC-calculated EFPS centerline and EFPS surface transient temperatures will also be referenced.

Table 4.3 contains, for all TRS cases, the radially dependent first-order time constants (as determined by the previously mentioned method) for the EFPS centerline and the EFPS surface. Also included in Table 4.3 are the uncertainties (derived from the calculational timestep size) for each time constant and the transient value of the heat transfer coefficient for each TRS case.

Additionally, the fifth through the second outermost nodal COM temperatures were analyzed for cases TRS03, TRS09, TRS13, TRS21, and TRS23 through TRS30, with their associated radially dependent first-order time constants presented in Table 4.4. These time constants have the same uncertainties as listed in Table 4.3 for the corresponding TRS case.

Table 4.3. EFPS centerline and EFPS surface first-order time constants with associated uncertainty for all TRS cases[a]

TRS case No.	EFPS centerline time constant (s)	$\tau(0)$ uncertainty (s)	EFPS surface time constant (s)	$\tau(r_{surf})$ uncertainty (s)	Heat transfer coefficient for $t > 0$ [kW/(m^2·K)]
1	17.87	+0.01	16.60	+0.01	0.5677
2	9.77	+0.01	8.27	+0.01	1.1354
3	7.07	+0.01	5.48	+0.01	1.7030
4	4.92	+0.01	3.20	+0.01	2.8384
5	4.01	+0.01	2.20	+0.01	3.9738
6	3.33	+0.01	1.42	+0.01	5.6768
7	2.80	+0.01	0.81	+0.01	8.5152
8	2.54	+0.01	0.50	+0.01	11.3536
9	2.28	+0.01			17.0304
10	2.15	+0.01			22.7072
11	2.08	+0.01			28.3840
12	2.03	+0.01			34.0608
13	1.82	+0.01			170.3040
14			0.2287	+0.0001	17.0304
15			0.1279	+0.0001	22.7072
16			0.0835	+0.0001	28.3940
17			0.0601	+0.0001	34.0608
18			0.0460	+0.0001	39.7376
19			0.0253	+0.0001	56.7680
20			0.0074	+0.0001	113.5360
21			0.0031	+0.0001	170.3040
22			0.0013	+0.0001	227.0720
23	8.00	+0.01	6.01	+0.01	1.7030
24	2.28	+0.01	0.29	+0.01	17.0304
25	6.39	+0.01	4.80	+0.01	1.7030
26	2.00	+0.01	0.17	+0.01	17.0304
27	6.38	+0.01	4.76	+0.01	1.7030
28	2.03	+0.01	0.19	+0.01	17.0304
29	2.50	+0.01	1.53	+0.01	1.5048
30	2.44	+0.01	0.85	+0.01	18.7946

[a]The transient value of the heat transfer coefficient for each TRS case is included for reference purposes.

Table 4.4. Radially dependent first-order time constants (s) for selected TRS cases

Radial position	TRS case number										
	3	9	13/21	23	24	25	26	27	28	29	30
℄	7.07	2.28	1.82	8.00	2.28	6.39	2.00	6.38	2.03	2.50	2.44
10				6.64	1.12			5.47	1.02		0.82
11				6.53	0.96			5.34	0.86		0.84
12	6.15	1.18	0.69	6.40	0.80	5.56	1.09	5.20	0.70	1.45	0.85
13	6.04	1.02	0.52	6.18	0.51	5.43	0.94	4.83	0.39	1.48	0.85
14	5.92	0.85	0.35			5.30	0.77			1.50	
15	5.65	0.46	0.0538			4.99	0.38			1.52	
Surface	5.48	0.23	0.0031	6.01	0.29	4.80	0.17	4.76	0.19	1.53	0.85

An example of the actual calculations used in creating Tables 4.3 and 4.4 can be found in Table 4.5, which involves case TRS03. This table includes the following for the particular TRS case: (1) the radial position r for which the time constant was calculated; (2) the distance of this radial position below the surface of the EFPS; (3) the initial temperature T(r, 0) at the given radius; (4) the final temperature $T(r, \infty)$ at the given radius; (5) the difference in the final and initial temperatures at the given radius; (6) this difference multiplied by $(1.0 - e^{-1.0})$; (7) the theoretical value of the temperature $T_{theory}[r, \tau(r)]$ at the given radial position and at the time equal to the time constant value at that radial position; (8, 9) two successive timestep ORINC-calculated temperature-time combinations which bound $T_{theory}[r, \tau(r)]$ at the given radial position, and (10) the calculated value of the first-order time constant $\tau(r)$ at the given radius.

4.3 Time Response–Depth Composite Relationship

The radial time constant results which are summarized in Tables 4.3 and 4.4 indicate a relationship between the magnitude of the EFPS surface conditions and the magnitude of these radial time constants. Figure 4.3 portrays this relationship for cases TRS01 through TRS22 as an association between the transient heat transfer coefficient and the time constants for the EFPS centerline and surface. Figure 4.3 has the following characteristics.

There are two ranges of the heat transfer coefficient over which the log of the surface time constant is linear with respect to the log of the heat transfer coefficient: (1) for those values of the heat transfer coefficient greater than ~11.4 kW/(m^2·K) and (2) for those values of the heat transfer coefficient less than ~4 kW/(m^2·K). The time constant for the centerline of the EFPS is nowhere linear with respect to t[illegible]eat transfer coefficient, although it does appear to approach ~1.8 s asymptotically as the heat transfer coefficient becomes large. Because Fig. 4.3 represents the centerline and surface time constants, the time constants associated with any other radial position should lie within the envelope created by the surface and centerline time constants. Broadening of the envelope with increased heat transfer coefficient should be expected since (1) small heat transfer coefficients define a slow transient in which the centerline can respond equally with the surface and (2) large heat transfer coefficients define fast transients in which the energy transport capability of the EFPS dominates, thereby forcing the centerline to respond much more slowly than the surface. The envelope defined by the EFPS surface and centerline time constants appears to widen continually with increasing heat transfer coefficients; however, the difference in the surface and centerline time constants varies from ~1.3 s at low heat

Table 4.5. Critical information for determining radially dependent first-order time constants relative to case TRSO3

Nodal position	Radial position r (mm)	Distance from EFPS surface (mm)	T(r, 0) (K)	T(r, ∞) (K)	C_1 [T(r, ∞) − T(r, 0)] (K)	$C_2 = (0.63212)C_1$ (K)	$T_{theory}[r, \tau(r)] = T(r, 0) + C_2$ (K)	t (s)	$T_{ORINC}(r,t)$ (K)	t + Δt (s)	$T_{ORINC}(r,t + \Delta t)$ (K)	τ(r) (s)
[illegible]	0.0	5.38	532.91	299.67	−233.24	−147.44	385.47	7.07	385.56	7.08	385.41	7.07
12	4.38	1.00	530.45	299.67	−230.78	−145.88	384.57	6.15	384.65	6.16	384.51	6.15
13	4.64	0.74	529.72	299.67	−230.05	−145.42	384.30	6.04	384.34	6.0[illegible]	384.21	6.04
14	4.88	0.50	529.07	299.67	−229.40	−145.01	384.06	5.92	384.10	5.93	383.96	5.92
15	5.10	0.28	527.93	299.67	−228.26	−144.29	383.64	5.65	383.69	5.66	383.55	5.65
Surface	5.38	0.0	527.24	299.67	−227.57	−143.85	383.39	5.48	383.39	5.49	383.25	5.48

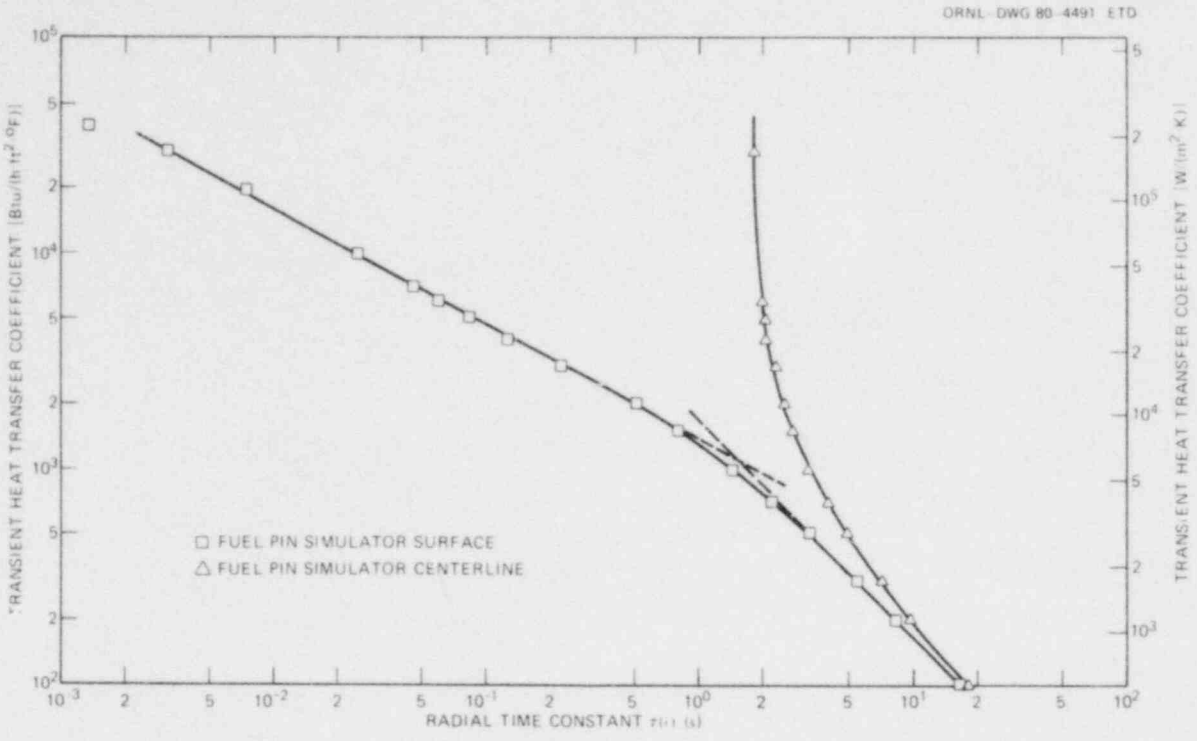

Fig. 4.3. Relationship between surface or centerline first-order time constants and transient heat transfer coefficients for cases TRS01 through TRS22.

transfer coefficients to ~2.0 s at intermediate heat transfer coefficients to ~1.8 s at high heat transfer coefficients.

In Sect. 4.2 the assumption was made that the EFPS is a first-order dynamic system. If this were the case, the relationship of Fig. 4.3 would be linear for both the surface and the centerline [an explanation of the linearity of the time constant–heat transfer coefficient relationship for first-order dynamic systems is given in the comments concerning the development from Eqs. (4.7) to (4.10)]. Because the time constant–heat transfer relationships of Fig. 4.3 clearly are not linear, additional explanation of the observed behavior of the EFPS is necessary.

The EFPS is in fact a complex interacting thermal system having a response function structure that must be obtained from mathematical modeling of the actual EFPS response characteristics. Because the radially dependent EFPS temperature is the response variable of interest, the response function structure of the EFPS is determined by making one-dimensional time-dependent energy balances on the concentric layers (one layer for each material) of a bundle 1 or bundle 2 EFPS[6] (see Fig. 1.2). This analysis, presented in Appendix B, produces expressions for the temperature perturbations of each concentric layer caused by a perturbation of the coolant bulk temperature.

The response of the temperature associated with the COM of the outer stainless steel sheath to a perturbation in the coolant temperature can be described by

$$T_B = -\left(\frac{R_{IS/OS}}{R_{OS/film}}\right)T_{IS} + \left(1 + \frac{R_{IS/OS}}{R_{OS/film}}\right)T_{OS} + \left(\frac{\gamma_{OS}}{R_{OS/film}}\right)\Delta T_{OS}\,, \qquad (4.5)$$

where

T_B = bulk coolant temperature,

T_{IS} = inner sheath temperature,

T_{OS} = outer sheath temperature,

γ_{OS} = capacitance of the outer sheath for thermal energy (see Appendix B),

$R_{i/j}$ = thermal resistance between i and j (see Appendix B),

Δ = differential operator.

Consider Eq. (4.5) with the assumption that $R_{OS/film} \gg R_{IS/OS}$. Thus, $R_{OS/film}$, which includes the heat transfer coefficient, is the dominant resistance to heat transfer associated with the EFPS. For this condition, the internal heat transfer resistances are not restrictive, and the EFPS interior can supply heat to the surface as quickly as the surface can dissipate it. Since

$$R_{OS/film} = \frac{2\pi\ell}{\{[\ln(r_{NOD6}/\bar{r}_{NOD6})]/K_{NOD6}\} + [1/hr_{NOD6}]} , \tag{4.6}$$

where

ℓ = axial length of EFPS,

r_{NOD6} = outer radius of EFPS,

$\bar{r}_{NOD6}$ = COM radius of outermost node in EFPS model,

K_{NOD6} = thermal conductivity of outermost node in EFPS model,

h = heat transfer coefficient,

and since for the current assumption $[\ln(r_{NOD6}/\bar{r}_{NOD6})]/K_{NOD6} \ll 1/hr_{NOD6})$, Eq. (4.5) can be reduced to the following:

$$T_B = \left[1 + \left(\frac{\gamma_{OS}}{h2\pi\ell r_{NOD6}}\right)\Delta\right]T_{OS} . \tag{4.7}$$

Equation (4.7) is a response function of the form that describes a first-order dynamic system. The time constant for this first-order system is defined as

$$\tau_{OS} = \frac{\gamma_{OS}}{h2\pi\ell r_{NOD6}} . \tag{4.8}$$

In the surface-resistance-dominated condition, the entire EFPS will respond essentially as defined by Eq. (4.7); therefore, γ_{OS} can be replaced by γ_{EFPS}, where γ_{EFPS} is the capacitance of the EFPS for thermal energy. Thus, expanding γ_{EFPS} into its components, Eq. (4.8) can be transformed into

$$\tau = \frac{(\rho C_p V)_{EFPS}}{h 2\pi \ell r_{surface}} \tag{4.9}$$

$[(\rho C_p V)_{EFPS} = \pi \ell \sum_{i=1}^{n} C_{p_i}(r^2_{outer_i} - r^2_{inner_i})$, where i is over n concentric layers]. Supplying numerical values for the physical property and geometric variables yields an equation that is linear with respect to

$$\tau = \frac{10.45}{h}, \tag{4.10}$$

where τ is in s and h is in $kW/(m^2 \cdot K)$. The prediction of Eq. (4.10) is overlaid on the results of Fig. 4.3 in Fig. 4.4. Equation (4.10) agrees very well in both slope and absolute value with the portion of the surface time constant curve associated with heat transfer coefficient values below ~4 $kW/(m^2 \cdot K)$.

As the EFPS heat transfer condition is transformed from being dominated by the heat transfer coefficient resistance to being dominated by an internally located thermal resistance, the surface will begin to respond much faster than predicted by Eq. (4.10). Therefore, in Fig. 4.4, the prediction of Eq. (4.10) will rotate counterclockwise as the heat transfer coefficient becomes large. This rotation will essentially pivot about the point on Fig. 4.4 defined by the time constant predicted by Eq. (4.10) corresponding to the heat transfer coefficient that is the upper bound for the surface-dominated heat transfer resistance condition (~4.0 $kW/(m^2 \cdot K)$. Above heat transfer coefficients of ~11.4 $kW/(m^2 \cdot K)$, the slope of the prediction of Eq. (4.10) tends to become less steep, thus approaching the slope of the

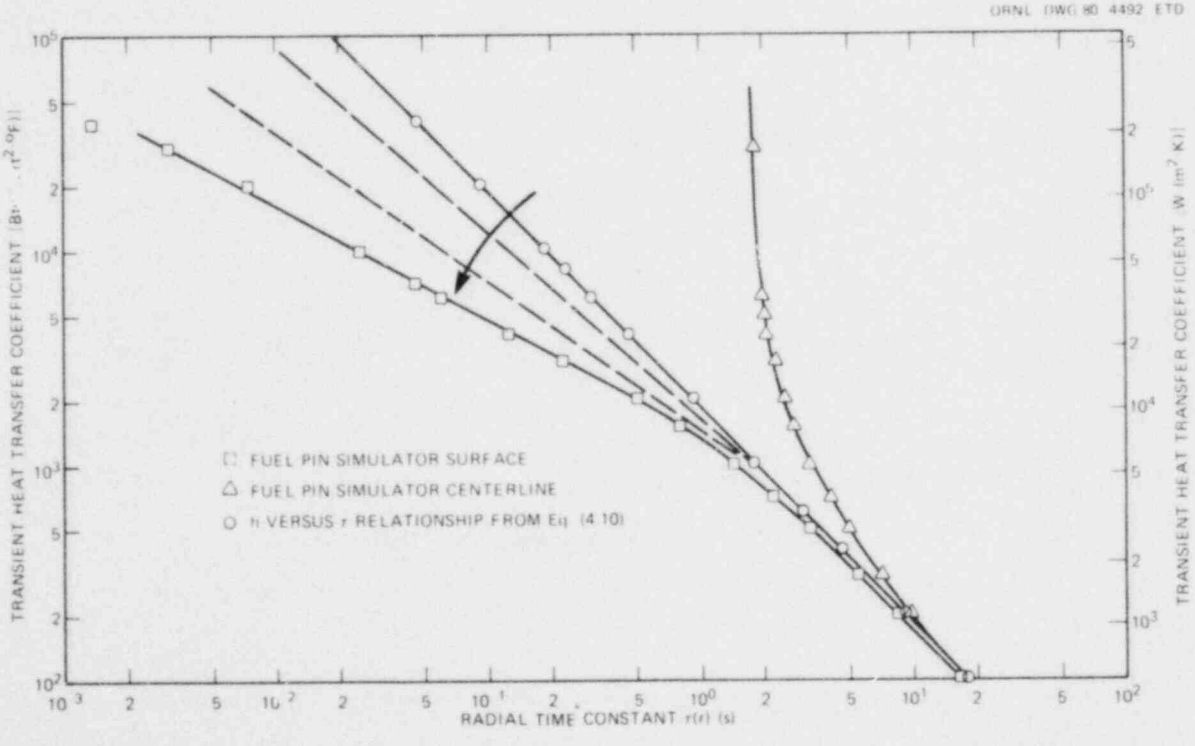

Fig. 4.4. Relationship between surface or centerline first-order time constants and transient heat transfer coefficients with prediction from Eq. (4.10).

upper linear portion of the observed surface time constant curve. Indeed, the conditions in which the heat transfer coefficient thermal resistance and the internally located thermal resistances are about equal define the transition area on Fig. 4.3 where the observed surface time constant curve is continuously changing slope (i.e., $\sim 4\ kW/(m^2 \cdot K) < h < \sim 11.4\ kW/(m^2 \cdot K)$).

The response of the centerline of the EFPS to a perturbation in the coolant temperature can be described by the following (see Appendix B):

$$T_B = [\xi_5\Delta^5 + \xi_4\Delta^4 + \xi_3\Delta^3 + \xi_2\Delta^2 + \xi_1\Delta + \xi_0]T_{MGO}\ , \tag{4.11}$$

where

Δ = differential operator,

T_B = bulk coolant temperature,

T_{MGO} = EFPS core temperature,

ξ_i = constants defined in Appendix B.

Equation (4.11) is a fifth-order response function for the centerline temperature of the EFPS; therefore, no linear portions of the centerline time constant curve should appear in Fig. 4.3.

For the EFPS heat transfer condition in which the restrictive thermal resistance is located within the MGO core (this case occurs as the heat transfer coefficient becomes large), the centerline response will be totally independent of the surface conditions. Thus, the time constant for the centerline will asymptotically approach a minimum value as the heat transfer coefficient increases. The value of the centerline time constant asymptote is from Eq. (4.11) to be

$$\tau_{\ell\,ASY} = \frac{\gamma_{MGO}}{R_{\ell/MGO}} = \frac{\rho_{MGO}C_{PMGO}\pi\ell(r_{MGO}^2)}{2\pi\ell(2K_{MGO}r_{MGO}^2)/(r_{MGO}^2)}\ , \tag{4.12}$$

which can be reduced to

$$\tau_{\ell\,ASY} = \frac{\rho_{MGO}C_{PMGO}r_{MGO}^2}{4K_{MGO}}\ , \tag{4.13}$$

where

γ_{MGO} = capacitance of the MGO core for thermal energy,

$R_{\ell/MGO}$ = thermal resistance between ℓ and MGO outer radius,

ℓ = axial length of EFPS,

ρ_{MGO} = density of MGO core,

C_{PMGO} = specific heat of MGO core,

r_{MGO} = outer radius of MGO core,

K_{MGO} = thermal conductivity of MGO core.

Substitution of the appropriate physical properties and geometric constants into Eq. (4.13) yields

$$\tau_{\text{EASY}} = 1.82 \text{ s} . \tag{4.14}$$

This result compares extremely well with the centerline time constant asymptote of Fig. 4.3.

Higher-order response theory has been applied to the EFPS to verify that the relationships of Fig. 4.3, which were obtained from first-order response theory, effectively explain the time-response characteristics of EFPS. Comparisons of the first-order results of Fig. 4.3 with calculated predictions of Eqs. (4.10) and (4.14) in general trends, slopes of linear sections, and time constants approached as the heat transfer coefficient becomes large or small indicate that first-order theory is sufficient to determine dependent time constants associated with certain heat transfer coefficient ranges.

The observation was made concerning Fig. 4.3 that the time constants for radial positions between the centerline and the surface of the EFPS should lie within the envelope of Fig. 4.3. However, the EFPS can experience a heat transfer condition for which this is not the case. If the dominant restriction to heat transfer in the EFPS is a heat transfer resistance associated with a radial position within the outer region of the heating element (large heat transfer coefficients), a situation arises where, in order to meet the boundary conditions on the surface, energy is removed from the mid-radius nodes (via conduction through the outer-radius nodes) faster than energy is supplied to the mid-radius nodes from the core region. Figure 4.5 is a representation of the radially dependent time constants for an EFPS

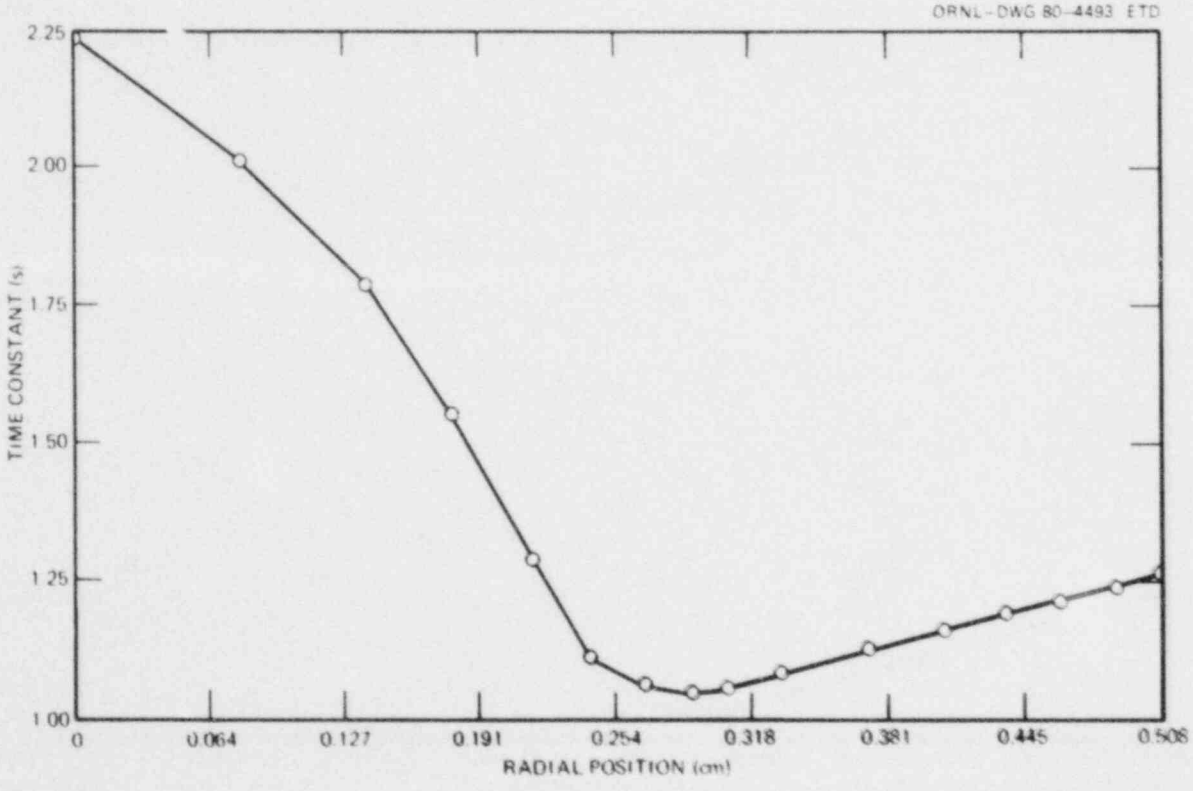

Fig. 4.5. Representation of radially dependent first-order time constants for a cooling EFPS experiencing a dominating surface-heat-flux driving potential.

experiencing this condition. The time constants at the mid-radius nodes are less than the time constant of the surface. This relation indicates that, for any given time, the internal radial positions are not lower in temperature than the surface, but rather, in relation to their steady-state temperature, their time constant temperatures $\{T[r, \tau(r)]\}$ are attained before the surface reaches its time constant temperature.

The condition for which the internal time constants are smaller than the surface time constant occurs in certain limiting cases where there is a large surface heat flux, which can be due to a large difference in the sink and surface temperatures and/or a large heat transfer coefficient. This surface heat flux creates a large driving potential near the surface of the EFPS, thereby forcing a significant amount of energy out of the surface. The MGO core region of the EFPS has a low thermal conductivity and thus cannot supply energy (the power generation rate is zero for $t > 0$ s) to the mid-radius nodes as quickly as energy is being drawn from them by the large surface driving potential and high thermal conductivity of the stainless steel sheaths. Therefore, the temperatures corresponding to the mid-radius nodal COMs are depressed and reach their time constant temperatures prematurely, with the result of smaller values for the internal radial time constants. Surface heat fluxes of such magnitude are not unusual but may occur frequently in loss-of-coolant experiments.

The test cases composing comparative groups one, two, and three have centerline and surface time constants presented in Table 4.3. These values can be overlaid on Fig. 4.3 to illustrate that the EFPS geometry associated with a particular axial power zone and the type of transient (i.e., heating or cooling) do not significantly affect the time constant–heat transfer coefficient relationship.

Comparative group four, however, is included to show that the initial conditions as well as the type of transient to which the EFPS responds have a marked effect on the calculated time constants. Thus, the information in Fig. 4.3 is extremely dependent on the initial conditions and the forcing functions (i.e., heat transfer coefficient and coolant temperature); the results cannot be generalized into an all-encompassing explanation of the time constant–heat transfer coefficient relationship.

5. CONCLUSIONS AND RECOMMENDATIONS

The transient calculations presented in the 7 TFS cases and the 30 TRS cases reveal a dramatic effect on the ability of the thermocouple to resolve rapidly changing surface phenomena and a lesser effect on the time response of the thermocouple attributable to the variation of the radial location of the thermocouple bead in the EFPS (within 1.016 mm of the surface). Four factors dominate the temperature resolution capability of the thermocouple response: (1) the distance from the surface of the EFPS to the radial position of the thermocouple bead, (2) device uncertainty in the thermocouple itself, (3) the magnitude of the power generation rate of the EFPS, and (4) the magnitude of the change in surface conditions. Two factors dominate the time response of an internally located thermocouple bead: (1) the distance from the surface of the EFPS to the radial position of the thermocouple bead and (2) the magnitude of the surface heat flux of the EFPS.

The inability of the thermocouple bead to resolve high-frequency surface conditions when it is displaced from the surface is illustrated in Figs. 5.1 and 5.2, which show that a surface condition occurring at a period of 100 ms is decipherable only by a thermocouple bead located within (0.14) (5.385) = 0.754 mm of the surface for axial power zone I and within (0.10) (5.385) = 0.538 mm of the surface for axial power zone V. These results are made conservative by the introduction of the thermocouple standard deviation and by the relatively small amplitude of the heat transfer coefficient–step-wave boundary condition.

Because of the instrument uncertainty of the thermocouple response, the nodal COM temperature associated with the thermocouple bead must have a total cycle magnitude of at least 1.111 K to be resolvable. This magnitude is a result of the extent to which the heat transfer coefficient is changing; for this study this change is small as compared with those experienced in actual THTF tests. [The heat transfer coefficient in these study cases ranges between 34.55 kW/(m^2·K) and 103.6 kW/(m^2·K) for axial power zone I and between 6.235 kW/(m^2·K) and 18.709 kW/(m^2·K) for axial power zone V, as compared with varying several orders of magnitude in THTF tests. However, these case calculations do indicate the inability of the thermometry to allow the inverse-implicit ORINC to calculate a varying heat transfer coefficient within 50% of its true value for surface phenomena occurring at frequencies in the higher range of the case studies.] Therefore, the depth at which a thermocouple can resolve a given surface frequency (for this is a function of the total cycle magnitude), as well as the highest frequency that can be interpreted at a given radial position, is very much dependent on the thermocouple uncertainty.

The test cases presented for a thermocouple bead located 0.508 mm below the surface of the EFPS (bundle 1 design as compared with 0.635 mm for bundle 2 design) show that surface conditions having a period of >40 ms for axial power zone I and a period of >90 ms at axial power zone V are the only ones that can be effectively reproduced by supplying the recorded thermocouple signal to the inverse-implicit ORINC. Because the THTF data acquisition system records the thermocouple signal at 50-ms intervals, it is capable of resolving an oscillatory condition having a period of about 100 ms. Thus, the EFPSs as designed in bundle 1 have a resolution capability consistent with the THTF data acquisition system within axial power zones I and V.

The depth of the thermocouple bead below the surface of the EFPS also affects its time-response characteristics. Examination of the radially dependent time-response characteristics of the EFPS yields several important results:

1. Overall EFPS response (in all heat transfer regimes) cannot be predicted by first-order response theory.

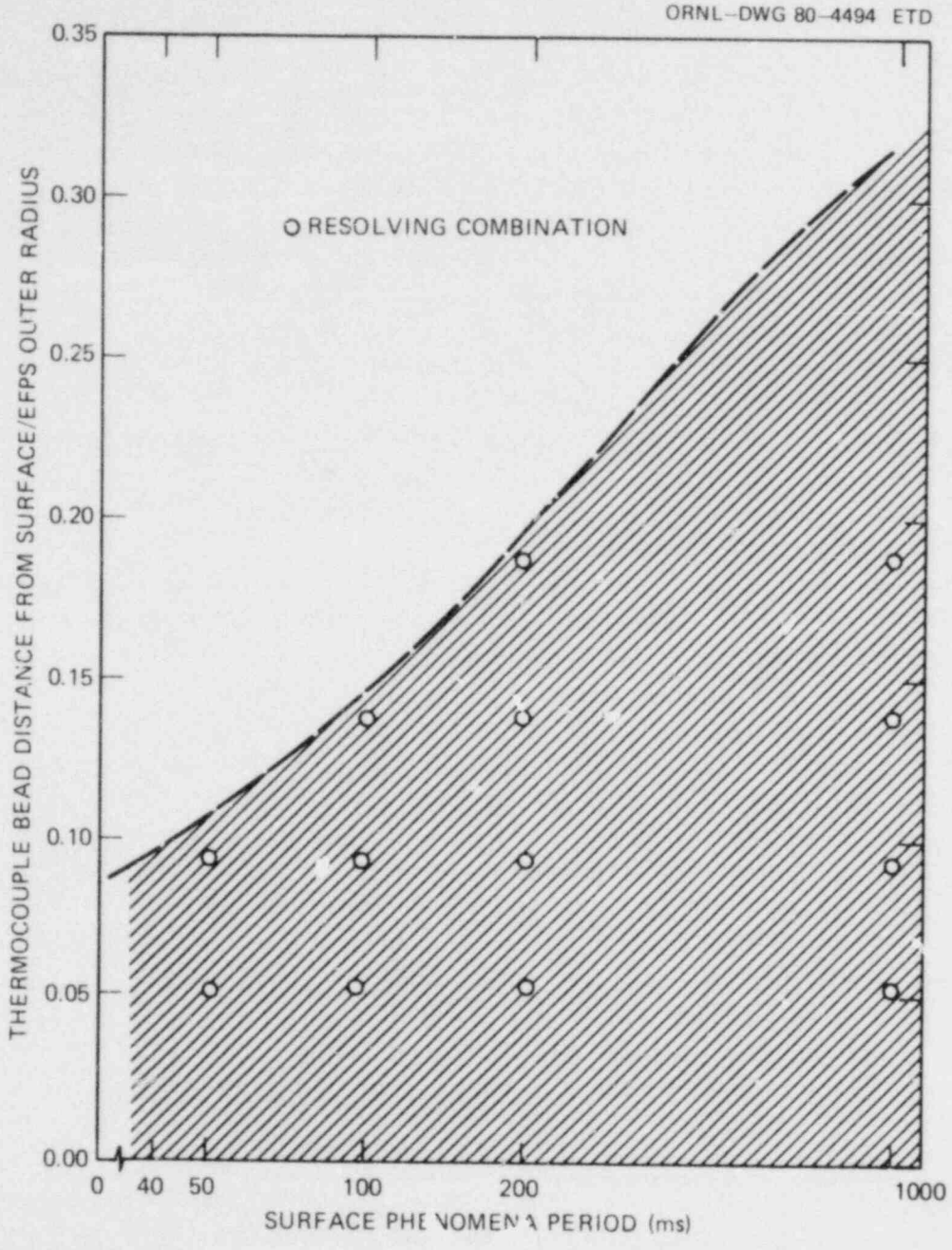

Fig. 5.1. Desirable combinations (represented by crosshatched area) of thermocouple bead depth and surface phenomenon period as determined by cases TFS1 through TFS7 involving axial power zone I.

2. For specific heat transfer coefficient ranges [$h < \sim 4\ kW/(m^2 \cdot K)$ and $h > 11.4\ kW/(m^2 \cdot K)$], the EFPS surface behaves in a first-order fashion.

3. In cases dominated by surface heat transfer resistance [$h < 4\ kW/(m^2 \cdot K)$], the EFPS time constant can be approximated by

$$\tau = [(\rho C_p V)_{EFPS}]/(h 2\pi \ell r_{surface}) ,$$

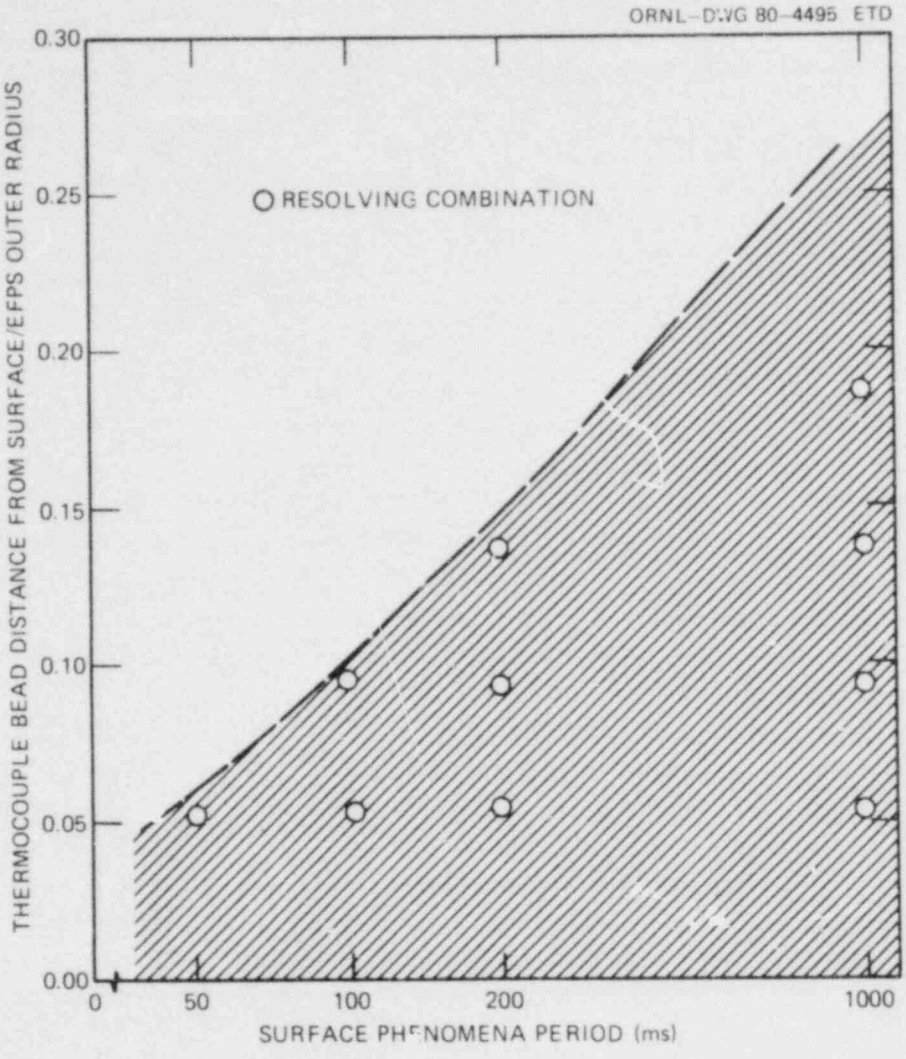

Fig. 5.2. Desirable combinations (represented by crosshatched area) of thermocouple bead depth and surface phenomenon period as determined by cases TFS1 through TFS7 involving axial power zone V.

where

$(\rho C_p V)_{EFPS}$ = capacitance of EFPS for thermal energy,

ℓ = axial length of EFPS,

$r_{surface}$ = outer radius of EFPS.

(Even for these cases, the differences between the centerline and surface response times are 1.3 to 2.0 s.)

4. When an internal thermal resistance dominates [$h > \sim 11.4$ kW/(m^2·K)], the EFPS surface responds much faster than predicted by the above equation, and the centerline response appears to be totally independent of the heat transfer coefficient.

5. The centerline response is multiorder, but for high surface heat transfer coefficients the centerline response time asymptotically approaches

$$\tau_{\ell} = \rho_{MGO}\, C_{PMGO} r_{MGO}^{2} / (4K_{MGO}) ,$$

where

ρ_{MGO} = density of MGO core,

C_{PMGO} = specific heat of MGO core,

r_{MGO} = outer radius of MGO core,

K_{MGO} = thermal conductivity of MGO core.

6. In certain situations—defined by high surface heat fluxes—the first-order response times of radial positions inside the EFPS are shorter than the EFPS surface response time.

7. The EFPS response is highly dependent on initial conditions and on the combination of forcing functions at the surface (i.e., heat transfer coefficient and sink temperature).

8. The EFPS response is not strongly dependent on the change in EFPS geometries from one axial power zone to another axial power zone.

These results indicate that first-order response theory should not be used for the analysis of EFPS transients and that first-order time constants (although they are correct for certain heat transfer conditions and EFPS radii) applied to the investigation of the complete thermal behavior of an EFPS are meaningless. Therefore, a thorough time-response analysis of the EFPS transients must be conducted with the rigorous solution of the transient heat conduction equation.

In general, the time response of the nodal positions in the radial vicinity where the thermocouple might be located will be negligible because the surface heat flux is often large enough to produce the dominating driving potential, which forces these nodes to have responses almost identical to the surface. Thus, for a thermocouple bead located within 1.016 mm of the surface of the EFPS, the thermocouple time response is much less restricting than the thermocouple resolving ability.

These conclusions make clear that the uncertainty of the thermocouple signal uncertainty limits its ability to resolve high-frequency boundary phenomena. Therefore, not only should future EFPSs be designed with the thermocouple positioned as close to the surface as mechanically possible, but an extensive effort should be undertaken to determine more accurately and/or to reduce the thermocouple uncertainty.

REFERENCES

1. *Project Description ORNL-PWR Blowdown Heat Transfer Separate-Effects Program–Thermal Hydraulic Test Facility (THTF),* ORNL/NUREG/TM-2 (February 1976).

2. L. J. Ott and R. A. Hedrick, *ORINC—A One-Dimensional Implicit Approach to the Inverse Heat Conduction Problem,* ORNL/NUREG-23 (November 1977).

3. S. B. Cliff, *A Collection of FORTRAN Support Routines,* K/CSD/TM-20 (January 1978).

4. L. J. Ott and R. A. Hedrick, *ORTCAL—A Code for THTF Heater Rod Thermocouple Calibration,* ORNL/NUREG-51 (February 1979).

5. E. O. Doebelin, *Measurement Systems—Application and Design,* McGraw-Hill, New York, 1975.

6. P. W. Murrill, *Automatic Control of Processes,* International Textbook Company, Scranton, Pa., 1967.

APPENDIXES

Appendix A

A STEP-RESPONSE SOLUTION TO THE GOVERNING DIFFERENTIAL EQUATION OF A FIRST-ORDER DYNAMIC SYSTEM

An n*th* order system dynamic response can be modeled by the following ordinary differential equation with constant coefficients:

$$a_n \frac{d^n x_{out}}{dt^n} + a_{n-1} \frac{d^{n-1} x_{out}}{dt^{n-1}} + \ldots + a_1 \frac{dx_{out}}{dt} + a_0 x_{out} =$$

$$b_m \frac{d^m x_{in}}{dt^m} + b_{m-1} \frac{d^{m-1} x_{in}}{dt^{m-1}} + \ldots + b_1 \frac{dx_{in}}{dt} + b_0 x_{in} , \qquad (A.1)$$

where

a_i = constants, i = 0, 1, ..., n;

b_j = constants, j = 0, 1, ..., m;

t = time;

x_{out} = system response quantity;

x_{in} = system input quantity.

In simplifying Eq. (A.1) to model a first-order system, all a_i (i = 2, 3, ..., n) are set to zero and all b_j (j = 1, 2, 3, ..., m) are set to zero. This results in

$$a_1 \frac{dx_{out}}{dt} + a_0 x_{out} = b_0 x_{in} . \qquad (A.2)$$

Dividing Eq. (A.2) by a_0 yields

$$\frac{a_1}{a_0} \frac{dx_{out}}{dt} + x_{out} = \frac{b_0}{a_0} x_{in} , \qquad (A.3)$$

where

$a_1 / a_0 \equiv \tau$ = system time constant,

$b_0 / a_0 \equiv \theta$ = a constant defined by the system.

The system input and output quantities of interest for the EFPS, at a radial position r_0, are the sink temperature (because the power generation rate is zero, the EFPS will attempt to attain equilibrium with this quantity so that the initial and final temperatures at r_0 will equal the initial and final sink temperatures) and the transient temperature $T(r_0, t)$, resulting from the perturbation of the sink temperature, respectively. Equation (A.3) can now be written in the form necessary for this study,

$$\tau(r_0) \frac{dT_{x_{out}}(r_0, t)}{dt} + T_{x_{out}}(r_0, t) = \theta T_{x_{in}}(r_0, t) , \qquad (A.4)$$

where

$T_{x_{out}}(r_0, t)$ = the output system temperature at r_0 relative to $t = 0$,

$T_{x_{in}}(r_0, t)$ = the input system temperature at r_0 relative to $t = 0$,

$\tau(r_0)$ = the time constant associated with the radial position r_0.

The complete solution to Eq. (A.4) when $T_{x_{in}}(r_0, t)$ experiences a step of relative magnitude $T_{s_{in}}(r_0, t)$ [i.e., $T_{s_{in}}(r_0, t) = T(r_0, 0)$ for $t = 0$ and $T_{s_{in}}(r_0, t) = T(r_0, 0) + T_{CONSTANT}$ for $t > 0$] at time $t = 0$ can be found from the sum of the particular and homogeneous solutions to Eq. (A.4).

The solution to

$$\frac{dT_{x_{out}}(r_0, t)}{dt} + \frac{T_{x_{out}}(r_0, t)}{\tau(r_0)} = 0 \tag{A.5}$$

is of the form

$$S_{HOMOG} = A_1 e^{rt}, \tag{A.6}$$

where A_1 is a constant and r is given by the characteristic equation $r + 1/\tau(r_0) = 0$, which yields $r = -1/\tau(r_0)$ so that the solution to Eq. (A.5) is

$$S_{HOMOG} = A_1 e^{-t/\tau(r_0)}. \tag{A.7}$$

The particular solution to Eq. (A.4) can be found by the method of undetermined coefficients if the right side will yield a zero derivative upon sufficient differentiation. Because the right side of Eq. (A.4) is the input system quantity and this quantity is a step of relative magnitude $T_{s_{in}}(r_0, t)$ occurring at $t = 0$, for $t > 0$, $dT_{s_{in}}(r_0, t)/dt = 0$ because $T_{s_{in}}(r_0, t)$ equals a constant over this range of t. Therefore, the particular solution to Eq. (A.4) is of the form

$$S_{PART} = A_2 T_{s_{in}}(r_0, t) + A_3 \frac{dT_{s_{in}}(r_0, t)}{dt}. \tag{A.8}$$

The value of A_2 in Eq. (A.8) can be determined by substituting Eq. (A.8) into Eq. (A.4) and requiring Eq. (A.4) to be an identity. Namely,

$$\tau(r_0) \frac{d[A_2 T_{s_{in}}(r_0, t)]}{dt} + A_2 T_{s_{in}}(r_0, t) = \theta T_{s_{in}}(r_0, t), \tag{A.9}$$

which results in $A_2 = \theta$. Therefore,

$$S_{PART} = \theta T_{s_{in}}(r_0, t). \tag{A.10}$$

The combined solution to Eq. (A.4) is

$$T_{x_{out}}(r_0, t) = S_{PART} + S_{HOMOG} \tag{A.11}$$

or

$$T_{x_{out}}(r_0, t) = \theta T_{s_{in}}(r_0, t) + A_1 e^{-t/\tau(r_0)} . \tag{A.11A}$$

The value of A_1 can be found from the initial condition $T_{x_{out}}(r_0, t) = 0$ at $t = 0$ (since the system is initially at equilibrium), which yields $0 = \theta T_{s_{in}}(r_0, t) + A_1$ or $A_1 = -\theta T_{s_{in}}(r_0, t)$. The complete solution to Eq. (A.4) is then

$$T_{x_{out}}(r_0, t) = \theta T_{s_{in}}(r_0, t) - \theta T_{s_{in}}(r_0, t) e^{-t/\tau(r_0)} \tag{A.12}$$

or

$$T_{x_{out}}(r_0, t) = \theta T_{s_{in}}(r_0, t)[1.0 - e^{-t/\tau(r_0)}] \tag{A.12A}$$

for $t > 0$. Because $T_{x_{out}}(r_0, t)$ and $T_{s_{in}}(r_0, t)$ are the system input and ouput quantities relative to the temperature at r_0 and $t = 0$,

$$T_{x_{out}}(r_0, t) = T(r_0, t) - T(r_0, 0) , \tag{A.13}$$

and

$$T_{s_{in}}(r_0, t) = T(r_0, \infty) - T(r_0, 0) . \tag{A.13A}$$

Substituting Eqs. (A.13) and (A.13A) into Eq. (A.12A) ($\theta = 1$ from necessary relationship at $t = \infty$) results in

$$T(r_0, t) = T(r_0, 0) + [T(r_0, \infty) - T(r_0, 0)] [1.0 - e^{-t/\tau(r_0)}] . \tag{A.14}$$

Appendix B

THE DETERMINATION OF AN EFPS HIGHER-ORDER RESPONSE FUNCTION STRUCTURE

The higher-order response function structure for a bundle 1 or bundle 2 EFPS can be determined by performing one-dimensional time-dependent energy balances on the concentric layers of the EFPS defined according to material composition (see Figs. 1.2 and B.1). The energy balances for each concentric layer have this form:

$$q_{IN,i} - q_{OUT,i} + q_{GEN,i} = q_{ACC,i} , \tag{B.1}$$

where

$q_{IN,i}$ = rate of heat transfer into i*th* concentric layer,

$q_{OUT,i}$ = rate of heat transfer out of i*th* concentric layer,

$q_{GEN,i}$ = rate of heat generation in i*th* concentric layer,

$q_{ACC,i}$ = rate of accumulation of energy in i*th* concentric layer.

To simplify the analysis, each layer is assumed to be represented by only one temperature, and material physical properties as well as the EFPS geometry are assumed to be independent of time and temperature. Figure B.1 represents the resulting elementary model of the EFPS. The temperature of each layer is defined as that temperature occurring at the COM radius of that layer, $\bar{r}_i$; furthermore, the radii at which material interfaces occur are indicated by r_i.

The energy balance on the outer stainless steel sheath (OS) is

$$q_{IN,OS} - q_{OUT,OS} + q_{GEN,OS} = \rho_{OS} Cp_{OS} V_{OS} \frac{\partial T_{OS}}{\partial t} , \tag{B.2}$$

where

ρ_i = density of i*th* concentric layer,

Cp_i = specific heat of i*th* concentric layer,

V_i = volume of i*th* concentric layer,

T_i = temperature at center of mass of i*th* concentric layer,

t = time.

In a cylindrical coordinate system $q_{IN,OS}$ is represented as

$$q_{IN,OS} = -\left(\frac{2\pi\ell}{\{[\ln(\bar{r}_{NOD6}/r_{NOD5})]/K_{NOD6}\} + (\Omega_{IS/OS}) + \{[\ln(r_{NOD5}/\bar{r}_{NOD5})]/K_{NOD5}\}} \right)$$

$$\times (T_{OS} - T_{IS}) . \tag{B.3}$$

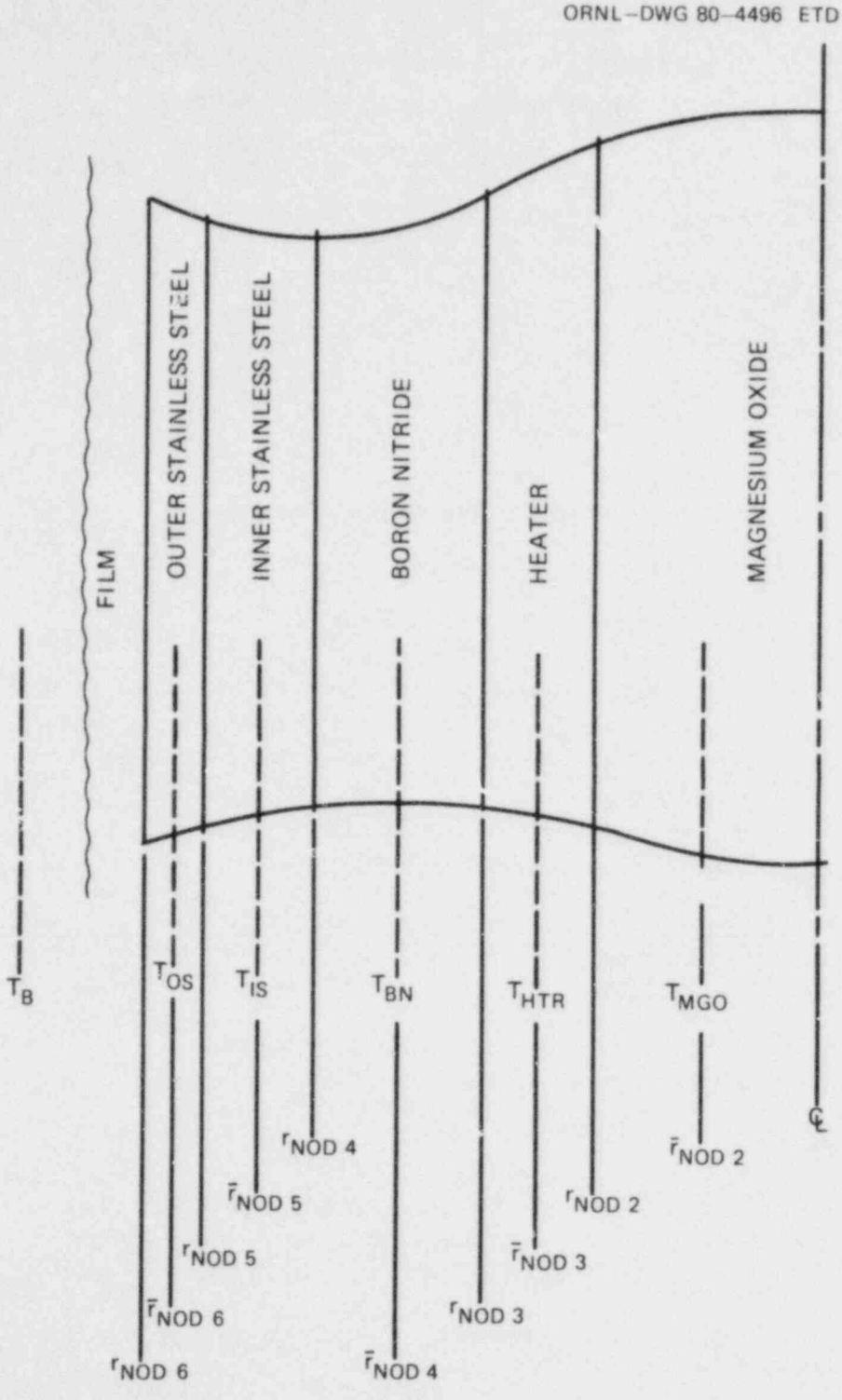

Fig. B.1. Simplified EFPS model used in determining higher-order response function structure.

Similarly, $q_{OUT,OS}$ is represented as

$$q_{OUT,OS} = -\left(\frac{2\pi\ell}{\{[\ln(r_{NOD6}/\bar{r}_{NOD6})]/K_{NOD6}\} + [1/(hr_{NOD6})]} \right) (T_B - T_{OS}) , \tag{B.4}$$

where

ℓ = axial length of EFPS,

K_m = thermal conductivity at radial position m,

$\Omega_{i/j}$ = interface resistance between *ith* and *jth* concentric layer,

h = heat transfer coefficient.

Let

$$\gamma_{OS} \equiv \rho_{OS} Cp_{OS} V_{OS} , \tag{B.5}$$

where γ_i is the capacitance of *ith* concentric layer for thermal energy. Define $R_{IS/OS}$ and $R_{OS/film}$ to be the square-bracketed terms in Eqs. (B.3) and (B.4), respectively. Equation (B.2) then can be reduced to

$$-R_{IS/OS}(T_{OS} - T_{IS}) + R_{OS/film}(T_B - T_{OS}) = \gamma_{OS}\Delta T_{OS} , \tag{B.6}$$

where Δ is a differential operator. The energy balance on the inner stainless steel sheath is

$$q_{IN,IS} + q_{GEN,IS} - q_{OUT,IS} = \rho_{IS} Cp_{IS} V_{IS} \frac{\partial T_{IS}}{\partial t} . \tag{B.7}$$

Letting

$$\gamma_{IS} \equiv \rho_{IS} Cp_{IS} V_{IS} \tag{B.8}$$

and

$$R_{BN/IS} = \left(\frac{2\pi\ell}{\{[\ln(\bar{r}_{NOD5}/r_{NOD4})]/K_{NOD5}\} + (\Omega_{IS/BN}) + \{[\ln(r_{NOD4}/\bar{r}_{NOD4})]/K_{NOD4}\}} \right) , \tag{B.9}$$

Eq. (B.7) can be reduced to

$$-R_{BN/IS}(T_{IS} - T_{BN}) + R_{IS/OS}(T_{OS} - T_{IS}) = \gamma_{IS}\Delta T_{IS} . \tag{B.10}$$

The final form of the energy balance on the BN insulator is

$$-R_{HTR/BN}(T_{BN} - T_{HTR}) + R_{BN/IS}(T_{IS} - T_{BN}) = \gamma_{BN}\Delta T_{BN} , \tag{B.11}$$

where

$$\gamma_{BN} \equiv \rho_{BN} C_{p_{BN}} V_{BN} \tag{B.12}$$

and

$$R_{HTR,BN} = \left(\frac{2\pi\ell}{\{[\ln(\bar{r}_{NOD4}/r_{NOD3})]/K_{NOD4}\} + (\Omega_{HTR/BN}) + [(r_{NOD3}^2 - \bar{r}_{NOD3}^2)/(2K_{NOD3}r_{NOD3}^2)]} \right). \tag{B.13}$$

The final form of the energy balance on the Inconel heater element is

$$-R_{MGO/HTR}(T_{HTR} - T_{MGO}) + R_{HTR/BN}(T_{BN} - T_{HTR}) = \gamma_{HTR}\Delta T_{HTR}\,, \tag{B.14}$$

where

$$\gamma_{HTR} \equiv \rho_{HTR} C_{p_{HTR}} V_{HTR} \tag{B.15}$$

and

$$R_{MGO,HTR} = \left\{ \frac{2\pi\ell}{[(\bar{r}_{NOD3}^2 - r_{NOD2}^2)/(2K_{NOD3}r_{NOD2}^2)] + (\Omega_{MGO/HTR}) + [(r_{NOD2}^2 - \bar{r}_{NOD2}^2)/(2K_{NOD2}r_{NOD2}^2)]} \right\}. \tag{B.16}$$

The final form of the energy balance on the MGO core is

$$R_{MGO/HTR}(T_{HTR} - T_{MGO}) = \gamma_{MGO}\Delta T_{MGO}\,, \tag{B.17}$$

where

$$\gamma_{MGO} \equiv \rho_{MGO} C_{p_{MGO}} V_{MGO}\,. \tag{B.18}$$

Solving Eqs. (B.6) through (B.17) for T_B, T_{OS}, T_{IS}, T_{BN}, T_{HTR}, respectively, yields

$$T_B = -\left(\frac{R_{IS/OS}}{R_{OS/film}}\right)T_{IS} + \left(1 + \frac{R_{IS/OS}}{R_{OS/film}}\right)T_{OS} + \left(\frac{\gamma_{OS}}{R_{OS/film}}\right)\Delta T_{OS}\,, \tag{B.19}$$

$$T_{OS} = -\left(\frac{R_{BN/IS}}{R_{IS/CS}}\right)T_{BN} + \left(1 + \frac{R_{BN/IS}}{R_{IS/OS}}\right)T_{IS} + \left(\frac{\gamma_{IS}}{R_{IS/OS}}\right)\Delta T_{IS}\,, \tag{B.20}$$

$$T_{IS} = -\left(\frac{R_{HTR/BN}}{R_{BN/IS}}\right)T_{HTR} + \left(1 + \frac{R_{HTR/BN}}{R_{BN/IS}}\right)T_{BN} + \left(\frac{\gamma_{BN}}{R_{BN/IS}}\right)\Delta T_{BN}\,, \tag{B.21}$$

$$T_{BN} = -\left(\frac{R_{MGO/HTR}}{R_{HTR/BN}}\right)T_{MGO} + \left(1 + \frac{R_{MGO/HTR}}{R_{HTR/BN}}\right)T_{HTR} + \left(\frac{\gamma_{HTR}}{R_{HTR/BN}}\right)\Delta T_{HTR}\,, \tag{B.22}$$

$$T_{HTR} = T_{MGO} + \left(\frac{\gamma_{MGO}}{R_{MGO/HTR}}\right)\Delta T_{MGO}\,. \tag{B.23}$$

Substituting Eq. (B.23) into Eq. (B.22) yields

$$T_{BN} = -\left(\frac{R_{MGO/HTR}}{R_{HTR/BN}}\right)T_{MGO} + \left[1 + \left(\frac{R_{MGO/HTR}}{R_{HTR/BN}}\right) + \left(\frac{\gamma_{HTR}}{R_{HTR/BN}}\right)\Delta\right] \times \left[1 + \left(\frac{\gamma_{MGO}}{R_{MGO/HTR}}\right)\Delta\right]T_{MGO} . \qquad (B.24)$$

Substituting Eqs. (B.24) and (B.23) into Eq. (B.21) yields

$$T_{IS} = -\left(\frac{R_{HTR/BN}}{R_{BN/IS}}\right)\left[1 + \left(\frac{\gamma_{MGO}}{R_{MGO/HTR}}\right)\Delta\right]T_{MGO} + \left[1 + \left(\frac{R_{HTR/BN}}{R_{BN/IS}}\right) + \left(\frac{\gamma_{BN}}{R_{BN/IS}}\right)\Delta\right] \times \left\{-\left(\frac{R_{MGO/HTR}}{R_{HTR/BN}}\right) + \left[1 + \left(\frac{R_{MGO/HTR}}{R_{HTR/BN}}\right) + \left(\frac{\gamma_{HTR}}{R_{HTR/BN}}\right)\Delta\right]\left[1 + \left(\frac{\gamma_{MGO}}{R_{MGO/HTR}}\right)\Delta\right]\right\}T_{MGO} . \qquad (B.25)$$

Substituting Eqs. (B.24) and (B.25) into Eq. (B.20) yields

$$T_{OS} = -\left(\frac{R_{BN/IS}}{R_{IS/OS}}\right)\left\{-\left(\frac{R_{MGO/HTR}}{R_{HTR/BN}}\right) + \left[1 + \left(\frac{R_{MGO/HTR}}{R_{HTR/BN}}\right) + \left(\frac{\gamma_{HTR}}{R_{HTR/BN}}\right)\Delta\right] \times \left[1 + \left(\frac{\gamma_{MGO}}{R_{MGO/HTR}}\right)\Delta\right]\right\}T_{MGO} + \left[1 + \left(\frac{R_{BN/IS}}{R_{IS/OS}}\right) + \left(\frac{\gamma_{IS}}{R_{IS/OS}}\right)\Delta\right] \times \left(-\left(\frac{R_{HTR/BN}}{R_{BN/IS}}\right)\left[1 + \left(\frac{\gamma_{MGO}}{R_{MGO/HTR}}\right)\Delta\right] + \left[1 + \left(\frac{R_{HTR/BN}}{R_{BN/IS}}\right) + \left(\frac{\gamma_{BN}}{R_{BN/IS}}\right)\Delta\right] \times \left\{-\left(\frac{R_{MGO/HTR}}{R_{HTR/BN}}\right) + \left[1 + \left(\frac{R_{MGO/HTR}}{R_{HTR/BN}}\right) + \left(\frac{\gamma_{HTR}}{R_{HTR/BN}}\right)\Delta\right]\left[1 + \left(\frac{\gamma_{MGO}}{R_{MGO/HTR}}\right)\Delta\right]\right\}\right)T_{MGO} . \qquad (B.26)$$

Substituting Eqs. (B.26) and (B.25) into Eq. (B.19) yields

$$T_B = \left\{-\left(\frac{R_{BN/OS}}{R_{OS/film}}\right)\left(-\left(\frac{R_{HTR/BN}}{R_{BN/OS}}\right)\left[1 + \left(\frac{\gamma_{MGO}}{R_{MGO/HTR}}\right)\Delta\right] + \left[1 + \left(\frac{R_{HTR/BN}}{R_{BN/IS}}\right) + \left(\frac{\gamma_{BN}}{R_{BN/IS}}\right)\Delta\right]\left\{-\left(\frac{R_{MGO/HTR}}{R_{HTR/BN}}\right) + \left[1 + \left(\frac{R_{MGO/HTR}}{R_{HTR/BN}}\right) + \left(\frac{\gamma_{HTR}}{R_{HTR/BN}}\right)\Delta\right] \times \left[1 + \left(\frac{\gamma_{MGO}}{R_{MGO/HTR}}\right)\Delta\right]\right\}\right) + \left[1 + \left(\frac{R_{IS/OS}}{R_{OS/film}}\right) + \left(\frac{\gamma_{OS}}{R_{OS/film}}\right)\Delta\right] \times \left[\left(\frac{R_{BN/IS}}{R_{IS/OS}}\right)\left(\frac{R_{MGO/HTR}}{R_{HTR/BN}}\right) - \left(\frac{R_{BN/IS}}{R_{IS/OS}}\right)\left[1 + \left(\frac{R_{MGO/HTR}}{R_{HTR/BN}}\right) + \left(\frac{\gamma_{HTR}}{R_{HTR/BN}}\right)\Delta\right] \times \left[1 + \left(\frac{\gamma_{MGO}}{R_{MGO/BN}}\right)\Delta\right] + \left[1 + \left(\frac{R_{BN/IS}}{R_{IS/OS}}\right) + \left(\frac{\gamma_{IS}}{R_{IS/OS}}\right)\Delta\right] \times \left(-\left(\frac{R_{HTR/BN}}{R_{BN/IS}}\right)\left[1 + \left(\frac{\gamma_{MGO}}{R_{MGO/HTR}}\right)\Delta\right] + \left[1 + \left(\frac{R_{HTR/BN}}{R_{BN/IS}}\right) + \left(\frac{\gamma_{BN}}{R_{BN/IS}}\right)\Delta\right] \times \left\{-\left(\frac{R_{MGO/HTR}}{R_{HTR/BN}}\right) + \left[1 + \left(\frac{R_{MGO/HTR}}{R_{HTR/BN}}\right) + \left(\frac{\gamma_{HTR}}{R_{HTR/BN}}\right)\Delta\right]\left[1 + \left(\frac{\gamma_{MGO}}{R_{MGO/HTR}}\right)\Delta\right]\right\}\right)\right]\right\}T_{MGO} . \qquad (B.27)$$

Equation (B.27) can be simplified, after multiplication of all of the terms, to the form

$$T_B = [\xi_5\Delta^5 + \xi_4\Delta^4 + \xi_3\Delta^3 + \xi_2\Delta^2 + \xi_1\Delta + \xi_0]T_{MGO}\,, \tag{B.28}$$

where ξ_i are constants that can be determined by reduction of Eq. (B.27); for example,

$$\xi_0 = 1 - \left(\frac{R_{MGO/HTR}}{R_{HTR/BN}}\right) - \left(\frac{R_{MGO/HTR}}{R_{BN/I}}\right) - \left(\frac{R_{HTR/BN}}{R_{IS/OS}}\right) - \left(\frac{R_{MGO/HTR}}{R_{HTR/BN}}\right) - \left(\frac{R_{IS/OS}}{R_{OS/film}}\right)$$

$$- \left(\frac{R_{MGO/HTR}}{R_{IS/OS}}\right) - \left(\frac{R_{MGO/HTR}}{R_{BN/IS}}\right)\left(\frac{R_{IS/OS}}{R_{OS/film}}\right) - \left(\frac{R_{HTR/BN}}{R_{OS/film}}\right) - \left(\frac{R_{MGO/HTR}}{R_{OS/film}}\right) \tag{B.29}$$

and

$$\xi_5 = \left(\frac{K_{OS}}{R_{OS/film}}\right)\left(\frac{K_{IS}}{R_{IS/OS}}\right)\left(\frac{K_{BN}}{R_{BN/IS}}\right)\left(\frac{K_{HTR}}{R_{HTR/BN}}\right)\left(\frac{K_{MGO}}{R_{MGO/HTR}}\right). \tag{B.30}$$

Arranging Eq. (B.28) into the Laplacian block-diagram form

$$\xrightarrow{T_B(S)} \boxed{\frac{1}{\xi_5\Delta^5 + \xi_4\Delta^4 + \xi_3\Delta^3 + \xi_2\Delta^2 + \xi_1\Delta + \xi_0}} \xrightarrow{T_{MGO}(S)} \tag{B.31}$$

immediately says that the response function for the EFPS is fifth-order in the MGO core.

NUREG/CR-1347
ORNL/NUREG-62
Dist. Category R2

Internal Distribution

1. M. Bender
2. R. E. Bohanan
3. W. G. Craddick
4–8. R. D. Dabbs
9. H. L. Falkenberry
10. R. M. Flanders
11. M. H. Fontana
12. U. Gat
13. R. C. Hagar
14. H. W. Hoffman
15. C. R. Hyman
16. A. F. Johnson
17. B. F. Maskewitz
18. R. W. McCulloch
19. D. G. Morris
20. F. R. Mynatt
21. L. J. Ott
22. J. L. Rich
23. J. P. Sanders
24. R. E. Textor
25. I. Spiewak
26. H. E. Trammell
27. D. B. Trauger
28. ORNL Patent Office
29. Central Research Library
30. Document Reference Section
31–32. Laboratory Records Department
33. Laboratory Records (RC)

External Distribution

34–35. Director, Division of Reactor Safety Research, Nuclear Regulatory Commission, Washington, DC 20555
36. Office of Assistant Manager for Energy Research and Development, DOE, ORO, Oak Ridge, TN 37830
37–38. Technical Information Center, DOE, Oak Ridge, TN 37830
39–423. Given distribution as shown in category R2 (NTIS-10)

☆U.S. GOVERNMENT PRINTING OFFICE: 1980-640-245/211